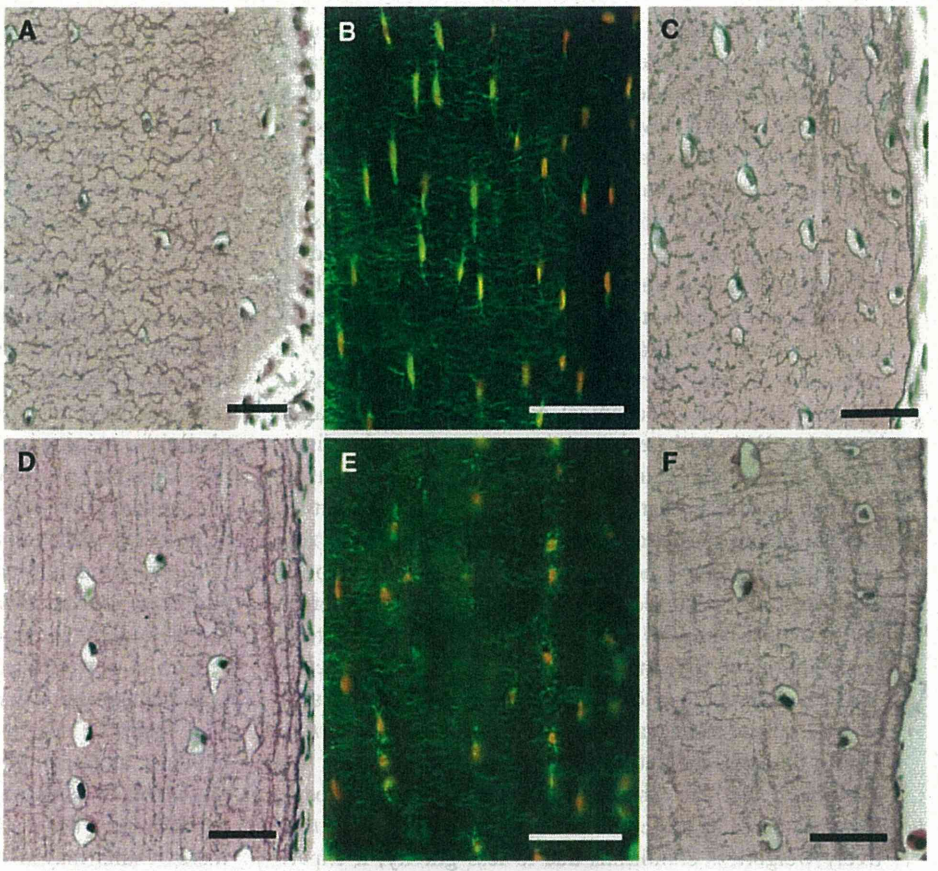

Fig. 5 Distribution of osteocytes and the lacunocanalicular system in the cortical bones of the femurs (**a**, **b**, **d**, **e**) and vertebrae (**c**, **f**) in four-toed tortoise (*Testudo horsfieldii*) (**a**–**c**) and green iguana (*Iguana iguana*) (**d**–**f**). Sections in **a**, **c**, **d**, and **f** were stained by Schoen's silver method, and those in **b** and **e** were stained with fluorescein-conjugated phalloidin. *Bars* 20 μm in **a**, **c**, **d** and **e**; 50 μm in **b** and **e**

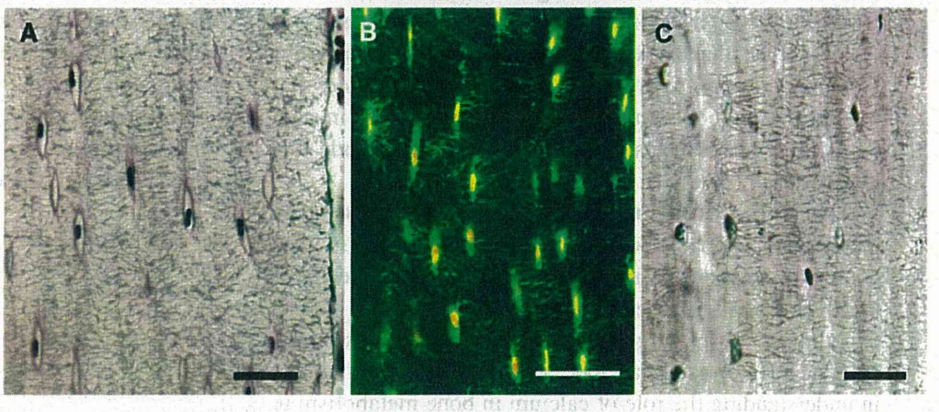

Fig. 6 Distribution of osteocytes and the lacunocanalicular system in cortical bone of the femur in mouse (**a**, **b**), and human (**c**). Sections in **a** and **c** were stained by Schoen's silver method, and that in **b** was stained with fluorescein-conjugated phalloidin. *Bars* 20 μm in **a** and **c**; 50 μm in **b**

connect with the adjacent osteocytes. On the other hand, thick and long cytoplasmic processes that were observed in the osteocyte lacunocanalicular system of other animals were rarely observed in zebrafish osteocytes by Schoen's silver staining, fluorescein-conjugated phalloidin staining, or electron microscopy (Figs. 1f, g, 2). The number of these cytoplasmic processes in zebrafish is limited to one or two in each osteocyte, while osteocytes in other animals exhibited numerous such structures. These results suggest that zebrafish bones have a poorly developed osteocyte lacunocanalicular system, compared to that in amphibians, reptiles, and mammals. Since zebrafish possess only the vertebral bone, we also compared the osteocyte lacunocanalicular system between vertebral bones and femurs in other animals. The vertebrae in these animals also retained well-developed osteocyte lacunocanalicular systems as well as femurs. These results indicate that a poorly developed osteocyte lacunocanalicular system in the zebrafish is not due to the difference between vertebral bone and long bone.

We showed the accumulation of an eosinophilic substance around some osteocytes in the sections of zebrafish

bones stained by Schoen's silver method. These structures might correspond to the amorphous substances with varying electron densities seen under the electron microscope. Since these structures were never observed in the osteocyte lacunae of *Xenopus laevis* and mouse, further studies are needed to reveal the nature of these substances.

Aquatic and land vertebrates live in different habitats. In this context, bones of these vertebrates are exposed to different mechanical strains and mineral acquisitions, both of which are important factors in regulating bone metabolism. Aquatic vertebrates are less affected by gravity as compared to land vertebrates. Since osteocytes play a central role in the mechanical adaptation of mammalian bones [1, 3], it will be interesting to compare the distribution of osteocytes and their lacunocanalicular systems between aquatic and land vertebrates. We revealed that the medaka has few osteocytes (acellular bone) and the zebrafish has apparent osteocytes (cellular bone) with a poorly developed osteocyte lacunocanalicular system. Interestingly, mature *Xenopus laevis*, which lives only in freshwater during its lifetime, exhibited numerous osteocytes and a well-developed osteocyte lacunocanalicular system as did the land vertebrates including *Rana nigromaculata*. These findings indicate that an aquatic habitat is not directly related to the development of an osteocyte lacunocanalicular system. Although the fish lives in relatively weightless conditions due to less gravity, it experiences mechanical strain during locomotion. Therefore, bones in teleost fishes may possess a mechanical sensing system other than osteocytes and the lacunocanalicular system. Although Witten and Huysseune suggested that osteoblasts and bone-lining cells might be involved in such a system [13], further studies are needed to conclude this hypothesis.

Bone plays vital roles in calcium and phosphate metabolism and is a reservoir of these minerals in land vertebrates; however, such functions in teleost bones have not been investigated extensively. In this context, Moss's experiments [24] using a fracture model of teleosts with cellular bone or acellular bone provide interesting findings in understanding the role of calcium in bone metabolism in teleost fishes. When goldfish (*Carassius auratus*), which has a cellular bone, and tilapia (*Tilapia macrocephala*), which has an acellular bone, were kept in calcium-depleted water, the goldfish formed a fracture callus composed of calcified cartilage and bone, but the tilapia formed uncalcified cartilage callus during fracture repair. These results suggest that calcium mobilization from bone is limited in teleost fishes with acellular bones and supports the idea that osteocytes play some role in calcium mobilization.

We conducted a comparative study on the morphology of the osteocyte lacunocanalicular system in the bones of various vertebrates by using Schoen's silver staining and fluorescein-conjugated phalloidin methods. In zebrafish bones, we observed fine and short cytoplasmic processes extending from the osteocytes in the fluorescein-conjugated phalloidin stained specimens, but not in the Schoen's silver-stained sections. These results suggest that fluorescein-conjugated phalloidin staining is more sensitive in detecting fine osteocyte cytoplasmic processes than Schoen's silver staining method. In the bones of other vertebrates, fluorescein-conjugated phalloidin staining clearly demonstrated an osteocyte lacunocanalicular system. Furthermore, this staining also allows observation of the three-dimensional structure of the osteocyte lacunocanalicular system under a confocal laser microscope. Thus, fluorescein-conjugated phalloidin staining is a useful technique to observe details of the osteocyte lacunocanalicular system.

Our study revealed that amphibians and land vertebrates possess a well-developed osteocyte lacunocanalicular system. Among amphibians, femurs of frogs (*Xenopus laevis* and *Rana nigromaculata*) exhibited osteocyte lacunocanalicular systems arranged perpendicular to the long axis, but femurs of newts (*Cynops pyrrhogaster*) showed a random arrangement of the osteocyte lacunocanalicular system. This might be due to the different maturation stage of the animals, because Hirose et al. [22] reported that the alignment of osteocyte lacunocanalicular systems changed depending on the maturation stages of mice. Alternatively, these results may also suggest that the alignment of the osteocyte lacunocanalicular systems may differ among the various species of vertebrates. In this context, further studies on the structure of osteocyte lacunocanalicular systems of various vertebrates, including the different developmental stages of each species, will provide more information and help to understand the phylogenic development and function of osteocytes.

Acknowledgments We thank Dr. Shizuko Ichinose and Dr. Akiko Himeno for their technical assistance. This work was supported by Grant-in-Aid for Scientific Research from the Japan Society for the Promotion of Science (14104015 and 22249061 to A.Y. and 21659426 to T.I.) and by a grant from the Japanese Ministry of Education, Global Center of Excellence (GCOE) Program, "International Research Center for Molecular Science in Tooth and Bone Diseases".

References

1. Bonewald LF (2006) Mechanosensation and transduction in osteocytes. Bonekey Osteovision 3:7–15
2. Tatsumi S, Ishii K, Amizuka N, Li M, Kobayashi T, Kohno K, Ito M, Takeshita S, Ikeda K (2007) Targeted ablation of osteocytes induces osteoporosis with defective mechanotransduction. Cell Metab 5:464–475
3. Henriksen K, Neutzsky-Wulff AV, Bonewald LF, Karsdal MA (2009) Local communication on and within bone controls bone remodeling. Bone 44:1026–1033

4. Feng JQ, Ward LM, Liu S, Lu Y, Xie Y, Yuan B, Yu X, Rauch F, Davis SI, Zhang S, Rios H, Drezner MK, Quarles LD, Bonewald LF, White KE (2006) Loss of DMP1 causes rickets and osteomalacia and identifies a role for osteocytes in mineral metabolism. Nat Genet 38:1310–1315
5. Fukumoto S, Martin TJ (2009) Bone as an endocrine organ. Trends Endocrinol Metab 20:230–236
6. Shimada T, Kakitani M, Yamazaki Y, Hasegawa H, Takeuchi Y, Fujita T, Fukumoto S, Tomizuka K, Yamashita T (2004) Targeted ablation of Fgf23 demonstrates an essential physiological role of FGF23 in phosphate and vitamin D metabolism. J Clin Invest 113:561–568
7. Razzaque MS (2009) The FGF23-Klotho axis: endocrine regulation of phosphate homeostasis. Nat Rev Endocrinol 5:611–619
8. Toyosawa S, Shintani S, Fujiwara T, Ooshima T, Sato A, Ijuhin N, Komori T (2001) Dentin matrix protein 1 is predominantly expressed in chicken and rat osteocytes but not in osteoblasts. J Bone Miner Res 16:2017–2026
9. Weiss RE, Watabe N (1979) Studies on the biology of fish bone. III. Ultrastructure of osteogenesis and resorption in osteocytic (cellular) and anosteocytic (acellular) bones. Calcif Tissue Int 28:43–56
10. Peignoux-Deville J, Lallier F, Vidal B (1982) Evidence for the presence of osseous tissue in dogfish vertebrae. Cell Tissue Res 222:605–614
11. Ekanayake S, Hall BK (1987) The development of acellularity of the vertebral bone of the Japanese medaka, *Oryzias latipes* (Teleostei; Cyprinidontidae). J Morphol 193:253–261
12. Hughes DR, Bassett JR, Moffat LA (1994) Histological identification of osteocytes in the allegedly acellular bone of the sea breams *Acanthopagrus australis*, *Pagrus auratus* and *Rhabdosargus sarba* (Sparidae, Perciformes, Teleostei). Anat Embryol 190:163–179
13. Witten PE, Huysseune A (2009) A comparative view on mechanisms and functions of skeletal remodelling in teleost fish, with special emphasis on osteoclasts and their function. Biol Rev Camb Philos Soc 84:315–346
14. Miura S, Hanaoka K, Togashi S (2008) Skeletogenesis in *Xenopus tropicalis*: characteristic bone development in an anuran amphibian. Bone 43:901–909
15. Rubinacci A, Villa I, Dondi Benelli F, Borgo E, Ferretti M, Palumbo C, Marotti G (1998) Osteocyte-bone lining cell system at the origin of steady ionic current in damaged amphibian bone. Calcif Tissue Int 63:331–339
16. Anderson MP, Capen CC (1976) Fine structural changes of bone cells in experimental nutritional osteodystrophy of green iguanas. Virchows Arch B Cell Pathol 20:169–184
17. Zimmer C (2007) Evolution. Jurassic genome. Science 315:1358–1359
18. Pyati UJ, Webb AE, Kimelman D (2005) Transgenic zebrafish reveal stage-specific roles for Bmp signaling in ventral and posterior mesoderm development. Development 132:2333–2343
19. Inohaya K, Takano Y, Kudo A (2007) The teleost intervertebral region acts as a growth center of the centrum: in vivo visualization of osteoblasts and their progenitors in transgenic fish. Dev Dyn 236:3031–3046
20. Renn J, Winkler C (2009) Osterix-mCherry transgenic medaka for in vivo imaging of bone formation. Dev Dyn 238:241–248
21. Inohaya K, Takano Y, Kudo A (2010) Production of Wnt4b by floor plate cells is essential for the segmental patterning of the vertebral column in medaka. Development 137:1807–1813
22. Hirose S, Li M, Kojima T, de Freitas PH, Ubaidus S, Oda K, Saito C, Amizuka N (2007) A histological assessment on the distribution of the osteocytic lacunar canalicular system using silver staining. J Bone Miner Metab 25:374–382
23. Moss ML (1961) Studies of the acellular bone of teleost fish. I. Morphological and systematic variations. Acta Anat 46:343–362
24. Moss ML (1962) Studies of the acellular bone of teleost fish. II. Response to fracture under normal and acalcemic conditions. Acta Anat 48:46–60

Biochemical and Biophysical Research Communications 417 (2012) 765–770

Contents lists available at SciVerse ScienceDirect

Biochemical and Biophysical Research Communications

journal homepage: www.elsevier.com/locate/ybbrc

Structural differences in the osteocyte network between the calvaria and long bone revealed by three-dimensional fluorescence morphometry, possibly reflecting distinct mechano-adaptations and sensitivities

Akiko Himeno-Ando [a,b,c], Yuichi Izumi [b,c], Akira Yamaguchi [a,c,*], Tadahiro Iimura [a,c,*]

[a] Section of Oral Pathology, Graduate School of Medical and Dental Sciences, Tokyo Medical and Dental University, Japan
[b] Section of Periodontology, Graduate School of Medical and Dental Sciences, Tokyo Medical and Dental University, Japan
[c] Global Center of Excellence (GCOE) Program, International Research Center for Molecular Science in Tooth and Bone Diseases, Tokyo Medical and Dental University, Japan

ARTICLE INFO

Article history:
Received 30 November 2011
Available online 16 December 2011

Keywords:
Osteocyte
Fluorescence imaging
Morphometry
Shear stress

ABSTRACT

The structural features of osteocytes and their cellular process network are thought to allow for mechanotransduction from the bone tissue to these cells. This study applied three-dimensional fluorescence microscopy to fixed and decalcified bone specimens to quantitatively compare the osteocytes and their networks between mouse parietal bone and tibia that are physiologically enforced by distinct mechanical loads. The subsequent morphometric analysis by the surface rendering of osteocyte cell bodies revealed the tibia to have relatively enriched cytoplasm in the osteocyte cell body in comparison to the parietal bone. Furthermore, quantitative tracing of the cellular processes *in silico* demonstrated that the numbers of the cellular processes and their bifurcation points per osteocyte in the tibia were significantly higher than those in the parietal bone. Though the total length of the processes per osteocyte in the tibia was two times longer, its total surface area and total volume were smaller than those in the parietal bone, due to its thinner diameter. These architectural differences in the osteocytes and their networks are thus implicated in the adaptation to physiologically different loading, and may also induce distinct mechanosensitivities.

1. Introduction

Osteocytes are embedded in the hard bone matrix of the lacunae, and form an intercellular network by extending slender cellular processes within narrow bony tubes of the canaliculi [1–4]. This structure ensures intercellular communication among bone cells including osteoblasts and osteoclasts. Osteocytes account for 90–95% of all bone cells and they are thought to sense mechanical loads and accordingly transmit the signals to osteoblasts and osteoclasts through the osteocyte network, and thus regulate bone remodeling [5–10]. Osteocytes also play a key role in phosphate metabolism by producing an endocrine factor, fibroblast growth factor 23 (FGF23), whose target organ is the kidney [11].

How osteocytes sense external loads remains unknown; however, the mechano-transduction of physical loads to the bone tissue must be tightly influenced by the structural features of bone including the lacunocanalicular and osteocyte network. Loading-induced fluid flow through the canalicular network has been thought to result in a fluid shear stress on the surface of osteocyte processes [12]. The interaction of the pericellular matrix and the osteocyte cellular process could amplify the physiological amplitude of loads to the bone tissue, thus producing sufficient levels of force to induce cellular response [13–16].

The skeletal system contains bones that are inherently loaded by distinct mechanical force patterns [17,18]. Long bones are loaded predominantly along the longitudinal direction with much higher amplitude than flat bones such as calvariae that are loaded radially and tangentially by intracranial pressure and mastication. The human fibula is estimated to have a load that is nearly twice that of the skull bone [19]. Extracellular mechanical forces are coupled to the intracellular organization of the cytoskeleton that regulates cellular connections to other cells and the extracellular matrix, thus affecting cell shape and functional outputs [20,21]. This suggests that the morphology of osteocytes, the patterning of the osteocyte network and their function are determined by external loading whose directional patterns and amplitudes are physiologically different in each bone. It is, therefore, relevant and intriguing to quantitatively manifest the structural differences of osteocytes and the osteocyte networks in distinct bones such as parietal bone and tibia.

* Corresponding authors. Address: Section of Oral Pathology, Graduate School of Medical and Dental Sciences, Tokyo Medical and Dental University, 1-5-45 Yushima, Bunkyo-ku, Tokyo 113-8549, Japan. Fax: +81 3 5803 0188.
E-mail addresses: akira.mpa@tmd.ac.jp (A. Yamaguchi), iimura.gcoe@tmd.ac.jp (T. Iimura).

0006-291X/$ - see front matter © 2011 Elsevier Inc. All rights reserved.
doi:10.1016/j.bbrc.2011.12.031

This study applied three-dimensional fluorescence microscopy to fixed and decalcified bone specimens followed by surface rendering of osteocyte cell bodies and tracing of osteocyte cellular processes *in silico* for better imaging acquisition of the osteocyte network to compare the mouse parietal bone and tibia. These morphometric analyses revealed significant quantitative architectural differences in the osteocytes and their networks in these bones.

2. Materials and methods

2.1. Animals and preparation of skeletal tissues

Mice (laboratory strain C57BL6J) were purchased from a local distributor. The parietal bones and tibiae were dissected from 8-week-old mice after anesthetizing the animals with 0.1% ethylanthranilate. Bone specimens were fixed in 4% paraformaldehyde for 4 °C. The specimens were washed with phosphate-buffered saline, and decalcified in 20% ethylenediaminetetraaceticacid (EDTA) for 14 days for 4 °C. The decalcified specimens were embedded in an optimal cutting temperature (OCT) compound (Sakura Finetek, Tokyo, Japan) to obtain cryosections. Frontal sections of the parietal bones and longitudinal sections of tibiae (10–20 μm) were prepared, respectively. The subsequent observations were focused on the outer cortical plates of parietal bones and the diaphysis of tibiae.

2.2. Staining for actin filaments with fluorescent dye-conjugatedphal loidin

The specimens were stained with phalloidin AlexaFluor 488 (Invitrogen, Carlsbad, CA, USA) for visualizing actin-rich cell bodies and cellular processes, and BOBO-3 (Invitrogen) for counter staining of nuclear DNA with 20 μg/ml of RNAaseI (Invitrogen) at room temperature for 2 h, as previously described [22].

2.3. Confocal laser scanning images

Confocal optical sectioning was performed with a system of LSM5 Pascal5 confocal laser scanning microscopy (Carl Zeiss, Oberkochen, Germany) with a PlanFluor objective (63×, N.A. = 1.4). Two laser lines, 488 nmand 543 nm were used. The theoretical *xy*- and *z*-axes resolutions were 0.178 and 0.700 μm, respectively. The refraction index correction was 0.934. The frame size of the image was 146.2 × 146.2 μm with 512 × 512 pixels and 8-bit color depth. Pixel size was 0.286 μm. Confocal images were taken with a 0.29 μm step size for voxel sampling and then were processed four times with Kalman averaging.

2.4. Three-dimensional (3D) reconstruction followed by the morphom etry of osteocytes and the cellular network tracing in silico

The 3D structure of the osteocyte network was constructed from a z-series of CLS images using IMARIS software (Bitplane, Zürich, Switzerland). The diameters of the osteocyte cell body and point-to-point distances between osteocytes were measured using the Measurement Pro function of IMARIS by rotating the 3D-reconstructed images. The surface area and volume of single osteocytes were measured by surface rendering using the Surface function of IMARIS. The threshold for the surface rendering of osteocytes was determined by super imposing the surface images to the 3D-reconstructed images until these two images overlapped. Any cellular processes measuring less than 0.5 μm in diameter were excluded in this rendering to separate the cell body and cell processes. The Filament Tracer function of IMARIS was originally developed to analyze neurite morphology and designed to reconstruct 3D dendritic tree models. This software package was employed to obtain dendritic tree models of the osteocyte network and to quantitate the pattern of the osteocyte cellular processes by measuring the numbers of endpoints, branching points, segments between a branching point to another branching point, and the diameter, surface area and volume of each segment. The beginning point at each osteocyte was set in the 3D-reconstructed images to trace the cellular processes radiating from single osteocytes, and the endpoints of the cellular process were set in several different sizes of the diameter (0.2, 0.3, 0.4 and 0.5 μm). The average total length of the processes, the average surface area, the average volume, the average number of endpoints, the average number of branching points and the average number of segments per osteocyte were calculated by dividing each total value by the number of osteocytes analyzed.

2.5. Statistics

The mean values of the morphometric parameters were statistically analyzed using paired *t*-test. Differences were considered to be significant if $p < 0.01$.

3. Results

The decalcified parietal bones and tibiae of the 8-week-old mice stained by a fluorescent dye-conjugated phalloidin were scanned by the high-resolution optical slices of the confocal z-series, which clearly showed the presence of the intercellular osteocyte networks in parietal bone and tibia (Fig. 1A and B, respectively). The 3D reconstitution and the surface rendering of the osteocytes obtained from the confocal z-series images revealed the morphology of the osteocyte cell body in the parietal bone and tibia (Fig. 1C and D, respectively). The morphology of the osteocytes in the parietal bone appeared relatively spherical or oval shaped, whereas those in the tibia were elongated and spindle-shaped. This morphological distinction was quantitatively confirmed by determining the longest and shortest diameters in the 3D-reconstructed images (Table 1). The diameters of the osteocyte cell bodies in the parietal bone and tibiae ranged from 6.46 ± 0.39 to10.78 ± 0.37 μm, and from 5.71 ± 0.30 to 15.52 ± 0.92 μm, respectively. Though the shortest diameter showed no significant difference, the longest diameter of the osteocyte cell body in the tibia was 44% longer than that in the parietal bone. The ratio of the longest to the shortest diameter obviously demonstrated that the osteocytes in the tibia were more elongated than those in the parietal bones. The distances between neighboring osteocytes in the two types of bone showed no significant differences (Table 1). This study next analyzed the volume and the surface area of the osteocyte cell bodies (Table 1). The volume and the surface area of the tibial osteocytes were significantly higher than those of the parietal osteocytes. There was no significant difference in the nuclear volumes of both groups of the osteocytes (Fig. 1E and F), thus the ratios of the cellular volume was compared to the nuclear volume. This comparison demonstrated that the cytoplasmic volume in the tibial osteocytes was nearly 50% larger than that in the parietal osteocytes.

The osteocyte cellular processes were traced using the Filament Tracer function to quantitatively compare the intercellular osteocyte networks in the parietal bone and tibia. The beginning point at each single osteocyte was set in the 3D-reconstituted images, and the endpoint diameter of the cellular process was set in several different sizes (Fig. 2). Preliminary manual measurements of 3D-reconstructed images revealed the size of the cellular processes originating from the cell surface to range from approximately 0.8–0.5 μm in diameter, and that the size of recognizable slender

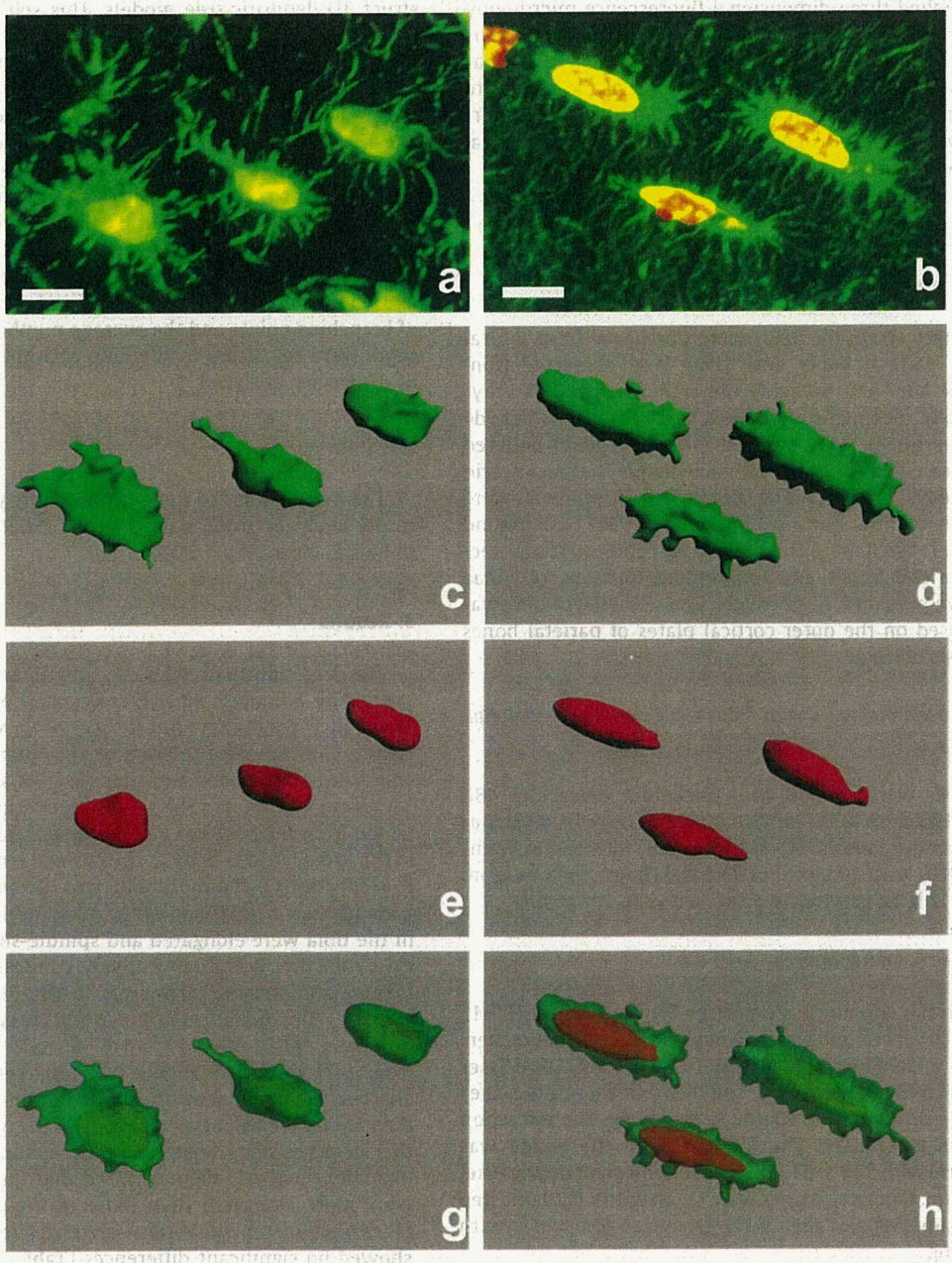

Fig. 1. Three dimensional (3D) reconstitution and surface rendering of osteocytes in the parietal bone (A, C, E and G) and tibia (B, D, F and H). The actin-rich cell body and cellular processes of osteocytes are visualized by a fluorescent dye-conjugated phalloidin (Pallioidin AlexaFluor 488) in green. Nuclei were conterstained by a cyanine nucleic acid dye (BOBO-3) in red. (A, B) Representative 3D-reconstituted images of the confocal z-series slices from parietal bone (A) and tibia (B) show osteocytes and theircellular process networks. Bar, 10 μm. (C, D) Surface renderings of osteocyte cell bodies of parietal bone (C) and tibia (D) from the 3D-reconstituted images (A and B, respectively) enable morphometric analyses (see Table 1). (E, F) Surface renderings of osteocyte nuclei of parietal bone (E) and tibia (F) from the 3D-reconstituted images (A and B, respectively) are shown. (G, H) Merged images (G and H) of the surface renderings of cell bodies and nuclei (C–E and D–F, respectively) are shown with 50% transparency of the cell bodies to visualize relative position of nucleus in cell body. (For interpretation of the references to colour in this figure legend, the reader is referred to the web version of this article.)

cellular processes forming the intercellular network and connections was nearly 0.2 μm in diameter. Therefore, the endpoints were set at 0.2, 0.3, 0.4 and 0.5 μm in diameter. Fig. 2 shows the dendritic tree models in different settings of the endpoint diameter. These tree models demonstrated that increasing number of the cellular processes and their bifurcations and more intensive and detailed appearances of the network were observed as the endpoint diameter setting got smaller in diameter. However, the settings of 0.2 and 0.3 μm in diameter revealed that the detailed rough surfaces of the osteocyte cell bodies that did not participate in the intercellular network were traced as the cellular processes. Furthermore, quite a few of the traced networks did not fit into the recognizable osteocyte network in the 3D-reconstructed images with connecting small separated fluorescence signals. Consistently, the quantification and statistical data at these settings often showed unreasonably small values in comparison to the actual

Table 1
Morphometric data of the osteocytes in mouse parietal bone and tibia.

	Parietal bone	Tibia
Shortest diameter (μm)	6.46 ± 0.39	5.71 ± 0.30
Longest diameter (μm)	10.78 ± 0.37	15.52 ± 0.92
Diameter ratio, long/short	1.67	2.67
Cell-cell distance (μm)	22.09 ± 1.30	21.06 ± 1.20
Cell volume (μm^3)	242.93 ± 21.63	413.25 ± 41.69
Cell surface area (μm^2)	279.41 ± 24.91	458.26 ± 53.60
Nuclear volume (μm^3)	115.74 ± 7.60	135.54 ± 11.94
Volume ratio, cell/nucleus	2.1	3.05

The values are the mean ± SEM of 20 osteocytes in each bone.
* $P < 0.01$.

resolution of this microscopy system and image processing (data not shown). Therefore, the osteocyte network was further evaluated by the endpoint setting at 0.4 μm in diameter.

This *in silico* tracing of the cellular processes by Filament Tracer function was used to calculate the average length, the average volume, the average surface area and the average diameter of each segment (Table 2). All the values exhibited significant differences indicating that the tibia has a thinner cellular process network with a higher branching rate, in comparison to the parietal bone. The numbers of endpoints, branching points and segments per osteocyte in the tibia revealed higher scores than those in the parietal bones, suggesting more a comprehensive network in the tibia (Table 3). The total length of the cellular processes per osteocyte

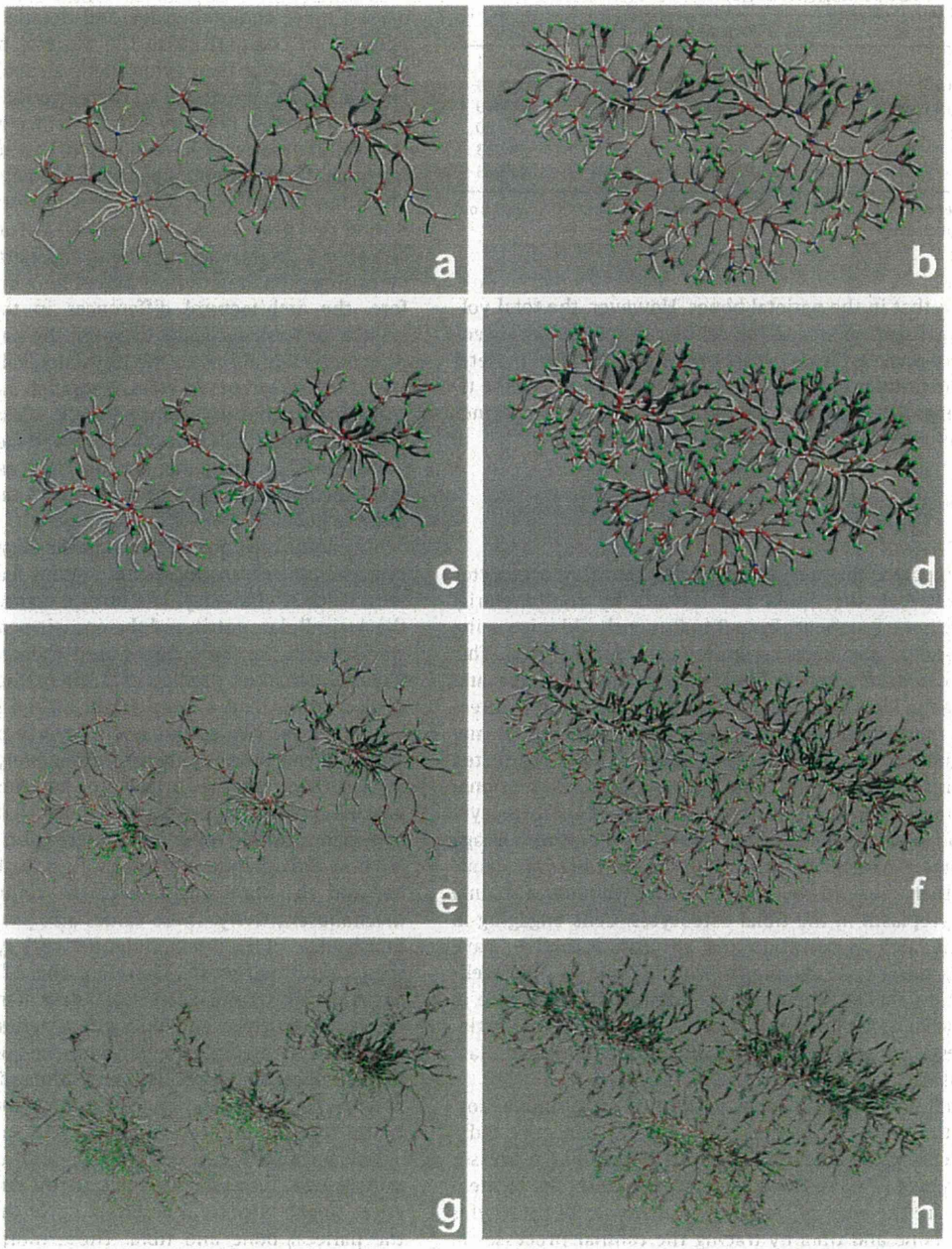

Fig. 2. Dendritic tree models of the osteocyte cellular processes in parietal bone (A, C, E and G) and tibia (B, D, F and H) from the 3D-reconstituted images (Fig. 1A and B, respectively). Dendritic tree models with different endpoint diameter settings at 0.5 μm (A and B), 0.4 μm (C and D), 0.3 μm (E and F) and 0.2 μm (G and H) are shown. Green dots, red dots and white bars indicate end points branching points and cellular process segments, respectively (see Tables 2 and 3). (For interpretation of the references to colour in this figure legend, the reader is referred to the web version of this article.)

Table 2
Morphometric values of the osteocyte networks in mouse parietal bone and tibia.

	Parietal bone	Tibia
Average length (μm)	2.57 ± 0.10	2.04 ± 0.05*
Average volume (μm³)	2.39 ± 0.18	0.36 ± 0.02*
Average surface area (μm²)	6.07 ± 0.35	2.26 ± 0.08*
Average diameter (μm)	0.95 ± 0.05	0.39 ± 0.01*

Average values per segment with the endpoint diameter setting at 0.4 μm are shown. A segment is defined as a cellular process segment from a branching point to another branching point or an endpoint. The values are the mean ± SEM.
* $P < 0.01$.

Table 3
Morphometric data of the osteocyte networks in mouse parietal bone and tibia (Total values of cellular processes per single osteocyte).

	Parietal bone	Tibia
Total length (μm)	311.06	637.67
Total volume (μm³)	288.87	112.49
Total surface area (μm²)	734.63	708.49
Total endpoints	64.00	162.00
Total branching point	58.00	152.33
Total segments	121.00	313.33

Total average values of cellular processes per single osteocyte were calculated from the values shown in Table 3.

was longer than that in the parietal bones. However, the total volume and the total surface area of the cellular processes per osteocyte in the tibia revealed lower scores than those in the parietal bone, due to the thinner diameter of the cellular process in the tibia. These findings indicated that the tibia has a longer and thinner intercellular network than that in the parietal bone.

4. Discussion

Vatsa et al. reported the morphometric differences in osteocytes and lacunae between the fibula and calvaria by combinatorial scanning of live bone fragments from 3 to 6-month-old mice using confocal microscopy and nano-computed tomography [23]. This revealed that osteocytes in the fibula had a spindle shape and stretched along the longitudinal axis of the principal loading direction, whereas those in the calvaria were spherical without any particular alignment in direction. The current study conducted two-color fluorescence morphometry by using three-dimensional confocal scanning followed by surface rendering of the osteocyte cell bodies and nuclei. This analysis revealed that the average volume and surface area of single osteocytes in the tibia was significantly larger than those in the parietal bone, which was mainly due to more cytoplasm in the tibial osteocytes. Cells engaging in active functions such as secretion and absorption tend to have relatively large volumes of cytoplasm probably due to their well-developed cell organelles. Therefore, the significant difference in the cytoplasmic volume of osteocytes between the tibia and parietal bone suggests a functional diversity in these cells to modulate bone metabolism.

A line of studies by Sugawara et al. performed quantitative morphometry for the cellular processes of osteocytes and provided a method to calculate the average length of the cellular processes per single osteocyte [24,25]. The current study attempted to measure and compare the sizes of the cellular processes of osteocytes in the parietal bone and tibia by tracing the cellular processes *in silico*. Considering the theoretical resolution of the microscopy system and the voxel size of the 3D reconstituted images, measurement of structures smaller than 0.4 μm was not expected to provide trust worthy data. In fact, the *in silico* tracings achieved by setting the endpoint at 0.3 and 0.2 μm did not fit for the visually recognizable network of the cellular process in the 3D reconstituted images. These settings revealed artificial connections of fluorescence signals that affected reasonable measurements. Though some part of the recognizable network smaller than 0.4 μm in diameter was not entirely traced, the morphometric analysis of the cellular processes revealed significant differences in the architectures of the osteocyte networks between the parietal bone and tibia.

The analysis revealed that osteocytes in the tibia radiate a significantly larger number of the cellular processes and branches in comparison to the parietal bone. Furthermore, the surface area and volume of each segment of the cellular process in the tibia was significantly smaller than those in the parietal bone, due to its smaller diameter. These data possibly indicate that tibia developed a more comprehensive and detailed osteocyte intercellular network in comparison to the parietal bone. Mechanical forces on cells influence their cytoskeletal structure, and thus their cellular shape and connection to the surrounding cells [20,21]. Immature osteocytes possibly align themselves and develop their intercellular network in response to distinct loading patterns during bone development, when they are being embedded in osteoid. The osteocyte cell body plays a key role for initial mechano-sensing during this process, as discussed by Vatsa et al. [23]. Hirose et al. reported a gradual arrangement and flattening of cortical osteocytes along the longitudinal axis of long bone with age [26]. Therefore, the architectural differences in the osteocytes and their cellular process networks between the parietal bone and tibia are probably adaptations to the physiologically different loading patterns. In our previous work, zebrafish have a poorly developed osteocyte lacunocanalicular network, whereas amphibians, reptiles and mammals all show well-developed lacunocanalicular systems, which could be intriguing because such osteocytic adaption to the mechanical loads might be involved in the phylogenetic diversity of bone [22].

The architectural differences in the network of osteocyte cellular processes may transduce extraosseous loads to cellular responses with distinct efficiency. The ultrastructure of osteocyte processes, the pericellular matrix and the encasing canaliculi provides the basic elements for fluid flow-based theoretical models [13,15,16]. Physical dynamics predicts that the extraosseous load could cause a shear strain and a hoop strain on the surface of the processes [12,13]. These two strains are in inverse proportion to the surface area and the inner diameter, respectively, in each basic physical model. Therefore, the surface area and the diameter of the cellular process could provide critical values with the mechanosensitivity of osteocytes. On the other hand, there is little view available regarding how the other quantitative values, such as the length, the number and the branching rate of the cellular processes affect the mechanosensitivity. These values also possibly reflect the comprehensiveness of the intercellular network system rather than simply the local ultrastructure. Therefore, these factors are likely to influence the cellular and intercellular flow of molecules associated with mechanosensitivity and biological functions [27]. The current findings collectively provoke views for the architectural differences in the osteocyte networks as the systems of molecular transduction and mechanotransduction, which may be associated with the functional diversity of the osteocyte itself.

In conclusion, our quantitative analyses based on the three-dimensional fluorescence microscopy revealed significant differences in the structural architecture of the osteocyte networks in the parietal bone and tibia. These morphometric differences in the osteocyte networks between flat bone and long bone probably reflect adaptations to different physiological loading patterns to these bones, and suggest different activities of the networks. The current analysis is therefore considered to provide new insights

into the physiological, pathological and phylogenetic mechanisms of mechanosensing and metabolism in bone [28,29].

Acknowledgments

The authors express sincere thanks to Ms. Kayoko Suenaga at Carl Zeiss MicroImaging Co., Ltd. for her valuable expertise on microscopy and image processing, and Drs Mayu Sugiyama and Hiroshi Kurokawa for their constructive comments on this work. The current work was supported by a grant from the Ministry of Education, Culture, Sports, Science, and Technology (MECSST), Global Center of Excellence (GCOE) Program, "International Research Center for Molecular Science in Tooth and Bone Diseases" to all the authors, a Grant-in-Aid for Scientific Research on Innovative Areas "Fluorescence Live imaging" (No. 22113002) of MECSST to T.I., and the Naito Foundation Subsidy for Promotion of Specific Research Projects (Osteobiology). A.Y. and T.I. were supported by a Grant-in-Aid for Scientific Research from the Japan Society for the Promotion of Science (JSPS). T. I. was also supported in part by the Takeda Science Foundation, the Mochida Memorial Foundation for Medical and Pharmaceutical Research, Yamada bee farm support project for honeybee research, and Grants H21-nanchi-097 and H22-nanchi-ippan157 from the Ministry of Health, Labor and Welfare.

References

[1] L.F. Bonewald, Osteocyte messages from a bony tomb, Cell Metab. 5 (2007) 410–411.
[2] L.F. Bonewald, Osteocytes as dynamic multifunctional cells, Ann. NY Acad. Sci. 1116 (2007) 281–290.
[3] L.F. Bonewald, The amazing osteocyte, J. Bone Miner Res. 26 (2011) 229–238.
[4] L.F. Bonewald, M.L. Johnson, Osteocytes, mechanosensing and Wnt signaling, Bone 42 (2008) 606–615.
[5] S. Tatsumi, K. Ishii, N. Amizuka, M. Li, T. Kobayashi, K. Kohno, M. Ito, S. Takeshita, K. Ikeda, Targeted ablation of osteocytes induces osteoporosis with defective mechanotransduction, Cell Metab. 5 (2007) 464–475.
[6] S.C. Cowin, L. Moss-Salentijn, M.L. Moss, Candidates for the mechanosensory system in bone, J. Biomech. Eng. 113 (1991) 191–197.
[7] E.H. Burger, J. Klein-Nulend, Mechanotransduction in bone-role of the lacuno-canalicular network, FASEB J. 13 Suppl (1999) S101–S112.
[8] T. Nakashima, M. Hayashi, T. Fukunaga, K. Kurata, M. Oh-Hora, J.Q. Feng, L.F. Bonewald, T. Kodama, A. Wutz, E.F. Wagner, J.M. Penninger, H. Takayanagi, Evidence for osteocyte regulation of bone homeostasis through RANKL expression, Nat. Med. 17 (2011) 1231–1234.
[9] J. Xiong, M. Onal, R.L. Jilka, R.S. Weinstein, S.C. Manolagas, C.A. O'Brien, Matrix-embedded cells control osteoclast formation, Nat. Med. 17 (2011) 1235–1241.
[10] C. Lin, X. Jiang, Z. Dai, X. Guo, T. Weng, J. Wang, Y. Li, G. Feng, X. Gao, L. He, Sclerostin mediates bone response to mechanical unloading through antagonizing Wnt/beta-catenin signaling, J. Bone Miner. Res. 24 (2009) 1651–1661.
[11] S. Fukumoto, T.J. Martin, Bone as an endocrine organ, Trends Endocrinol. Metab. 20 (2009) 230–236.
[12] K. Piekarski, M. Munro, Transport mechanism operating between blood supply and osteocytes in long bones, Nature 269 (1977) 80–82.
[13] Y. Han, S.C. Cowin, M.B. Schaffler, S. Weinbaum, Mechanotransduction and strain amplification in osteocyte cell processes, Proc. Natl. Acad. Sci. USA 101 (2004) 16689–16694.
[14] E.J. Anderson, S. Kaliyamoorthy, J. Iwan, D. Alexander, M.L. Knothe Tate, Nano-microscale models of periosteocytic flow show differences in stresses imparted to cell body and processes, Ann. Biomed. Eng. 33 (2005) 52–62.
[15] L. You, S.C. Cowin, M.B. Schaffler, S. Weinbaum, A model for strain amplification in the actin cytoskeleton of osteocytes due to fluid drag on pericellular matrix, J. Biomech. 34 (2001) 1375–1386.
[16] L.D. You, S. Weinbaum, S.C. Cowin, M.B. Schaffler, Ultrastructure of the osteocyte process and its pericellular matrix, Anat. Rec. A Discov. Mol. Cell Evol. Biol. 278 (2004) 505–513.
[17] M. Petrtyl, J. Hert, P. Fiala, Spatial organization of the haversian bone in man, J. Biomech. 29 (1996) 161–169.
[18] R. Hillam, M. Jackson, A. Goodship, and T. Skerry, Comparison of physiological strains in the human skull and tibia, Bone 19 (1) (1996) 686-686.
[19] K.L. Lambert, The weight-bearing function of the fibula. A strain gauge study, J. Bone Joint. Surg. Am. 53 (1971) 507–513.
[20] N. Wang, J.P. Butler, D.E. Ingber, Mechanotransduction across the cell surface and through the cytoskeleton, Science 260 (1993) 1124–1127.
[21] C.S. Chen, J. Tan, J. Tien, Mechanotransduction at cell-matrix and cell-cell contacts, Annu. Rev. Biomed. Eng. 6 (2004) 275–302.
[22] L. Cao, T. Moriishi, T. Miyazaki, T. Iimura, M. Hamagaki, A. Nakane, Y. Tamamura, T. Komori, A. Yamaguchi, Comparative morphology of the osteocyte lacunocanalicular system in various vertebrates, J. Bone Miner. Metab. (2011).
[23] A. Vatsa, R.G. Breuls, C.M. Semeins, P.L. Salmon, T.H. Smit, J. Klein-Nulend, Osteocyte morphology in fibula and calvaria – is there a role for mechanosensing?, Bone 43 (2008) 452–458
[24] Y. Sugawara, R. Ando, H. Kamioka, Y. Ishihara, T. Honjo, N. Kawanabe, H. Kurosaka, T. Takano-Yamamoto, T. Yamashiro, The three-dimensional morphometry and cell-cell communication of the osteocyte network in chick and mouse embryonic calvaria, Calcif. Tissue Int. 88 (2011) 416–424.
[25] Y. Sugawara, H. Kamioka, T. Honjo, K. Tezuka, T. Takano-Yamamoto, Three-dimensional reconstruction of chick calvarial osteocytes and their cell processes using confocal microscopy, Bone 36 (2005) 877–883.
[26] S. Hirose, M. Li, T. Kojima, P.H. de Freitas, S. Ubaidus, K. Oda, C. Saito, N. Amizuka, A histological assessment on the distribution of the osteocytic lacunar canalicular system using silver staining, J. Bone Miner. Metab. 25 (2007) 374–382.
[27] T. Adachi, Y. Aonuma, K. Taira, M. Hojo, H. Kamioka, Asymmetric intercellular communication between bone cells: propagation of the calcium signaling, Biochem. Biophys. Res. Commun. 389 (2009) 495–500.
[28] T. Iimura, A. Nakane, M. Sugiyama, H. Sato, Y. Makino, T. Watanabe, Y. Takagi, R. Numano, A. Yamaguchi, A fluorescence spotlight on the clockwork development and metabolism of bone, J. Bone Miner. Metab. (2011).
[29] R.P. van Hove, P.A. Nolte, A. Vatsa, C.M. Semeins, P.L. Salmon, T.H. Smit, J. Klein-Nulend, Osteocyte morphology in human tibiae of different bone pathologies with different bone mineral density – is there a role for mechanosensing?, Bone 45 (2009) 321–329

Laboratory Investigation (2012) 92, 688–702

Reduction of NOTCH1 expression pertains to maturation abnormalities of keratinocytes in squamous neoplasms

Kei Sakamoto[1], Takuma Fujii[2], Hiroshi Kawachi[3], Yoshio Miki[4], Ken Omura[5], Kei-ichi Morita[6], Kou Kayamori[7], Ken-ichi Katsube[1] and Akira Yamaguchi[1]

Notch is a transmembrane receptor functioning in the determination of cell fate. Abnormal Notch signaling promotes tumor development, showing either oncogenic or tumor suppressive activity. The uncertainty about the exact role of Notch signaling, partially, stems from inconsistencies in descriptions of Notch expression in human cancers. Here, we clarified basal-cell dominant expression of NOTCH1 in squamous epithelium. NOTCH1 was downregulated in squamous neoplasms of oral mucosa, esophagus and uterine cervix, compared with the normal basal cells, although the expression tended to be retained in cervical lesions. NOTCH1 downregulation was observed even in precancers, and there was little difference between cancers and high-grade precancerous lesions, suggesting its minor contribution to cancer-specific events such as invasion. In culture experiments, reduction of NOTCH1 expression resulted in downregulation of keratin 13 and keratin 15, and upregulation of keratin 17, and *NOTCH1* knockdown cells formed a dysplastic stratified epithelium mimicking a precancerous lesion. The NOTCH1 downregulation and the concomitant alterations of those keratin expressions were confirmed in the squamous neoplasms both by immunohistochemical and cDNA microarray analyses. Our data indicate that reduction of NOTCH1 expression directs the basal cells to cease terminal differentiation and to form an immature epithelium, thereby playing a major role in the histopathogenesis of epithelial dysplasia. Furthermore, downregulation of NOTCH1 expression seems to be an inherent mechanism for switching the epithelium from a normal and mature state to an activated and immature state, suggesting its essential role in maintaining the epithelial integrity.
Laboratory Investigation (2012) **92,** 688–702; doi:10.1038/labinvest.2012.9; published online 13 February 2012

KEYWORDS: epithelial dysplasia; esophagus; Notch1; oral mucosa; squamous cell carcinoma; uterine cervix; keratin

Notch is a transmembrane receptor that regulates cell proliferation and differentiation in various tissues. Notch is constitutively processed and is tethered on the plasma membrane as a heterodimeric protein, and the signal is transduced by the Notch intracellular domain (NICD) produced by ligand-induced cleavage,[1,2] which translocates to the nucleus and directly induces the transcription of downstream targets by forming a transactivation complex with several cofactors.[3] In humans, there are four *Notch* homologs (*NOTCH1*, *2*, *3*, *4*) and they exhibit diverse patterns of expression, suggesting different contributions in each tissue.

The expression of Notch1, Notch2 and Notch3 in mouse skin and hair follicles has been documented,[4–7] and Notch signaling seems to have important roles in the regulation of epidermal differentiation. Conditional knockout of *Notch1* in skin results in epidermal and corneal hyperplasia.[8] Overexpression of constitutively active Notch1 in basal cells leads to hyperplastic epidermis and abnormal hair development.[4,9] In contrast, deletion of *Notch2*, *Notch3* and *Notch4* does not cause significant changes in the epidermis.[6,10,11] These results indicate the significance of Notch1 in epidermal differentiation.

Abnormal Notch signaling can promote tumor development. The first indication that Notch has a role in carcinogenesis was obtained from a mouse mammary tumor virus integration assay in which four genes were identified as candidates that associate with tumor progression, the third of which (int-3) turned out to be a truncated form of *Notch4*.[12]

[1]Section of Oral Pathology, Tokyo Medical and Dental University, Tokyo, Japan; [2]Department of Obstetrics and Gynecology, Keio University School of Medicine, Tokyo, Japan; [3]Section of Human Pathology, Tokyo Medical and Dental University, Tokyo, Japan; [4]Section of Molecular Genetics, Medical Research Institute, Tokyo Medical and Dental University, Tokyo, Japan; [5]Section of Oral and Maxillofacial Surgery, Tokyo Medical and Dental University, Tokyo, Japan; [6]Department of Advanced Molecular Diagnosis and Maxillofacial Surgery, Hard Tissue Genome Research Center, Tokyo Medical and Dental University, Tokyo, Japan and [7]Section of Diagnostic Oral Pathology, Tokyo Medical and Dental University, Tokyo, Japan
Correspondence: Dr K Sakamoto, Section of Oral Pathology, Tokyo Medical and Dental University, Yushima 1-5-45, Tokyo 113-0034, Japan.
E-mail: s-kei.mpa@tmd.ac.jp

Received 29 August 2011; revised 25 November 2011; accepted 15 December 2011

Gain of function mutation of *NOTCH1* was detected in many cases of T-cell acute lymphoblastic leukemia,[13] and this finding gave rise to the concept of treatment by inhibiting the formation of Notch transactivation complex.[14] In cervical cancer, the upregulation of NOTCH1[15,16] and NOTCH2,[16] and an increase in nuclear localization of NICD[17] were documented. On the basis of these observations, activation of Notch signaling is thought to be associated with the development of cervical cancer.[18] However, promotion of carcinogenesis by Notch signal activation seems contradictory to the phenotypes observed in the *Notch1* knockout mouse, which exhibits an increase in the incidence of papilloma and chemical-induced skin cancer,[8] and the transgenic mouse of the pan-Notch inhibitor, dominant-negative *Mastermind-like 1*, which shows dysplasia and SCC of skin.[19] In fact, expression of NOTCH1 is decreased in skin cancer,[20,21] suggesting that *NOTCH1* acts as a tumor suppressor. To solve the discrepancy of the proposed role of Notch, accurate knowledge of its expression is crucial. To assess its contribution in cancer, the Notch expression should be evaluated in comparison with the normal cells from which the cancer cells originated. However, it appears that the expression of Notch in human cancers has not been properly evaluated along this line. Even the localization of Notch proteins in normal adult tissue is unclear, partially, because of the difficulty of detection.

To address this issue, we have engaged in an examination of Notch expression in adult human tissues. In this study, we first demonstrate that NOTCH1 is predominantly expressed in the basal cells of normal squamous epithelium. Then we expand the examination to neoplasms that have originated from squamous epithelium and show that Notch1 expression is downregulated in these lesions. Cell culture experiments indicate that reduction of NOTCH1 expression associates with abnormal differentiation represented by alteration of keratin subtype expression. Our data suggest that aberrant epithelial differentiation in squamous neoplasms is caused by the reduction of NOTCH1 expression, which in turn unveils its essential function in the maintenance of normal epithelial integrity.

MATERIALS AND METHODS

Clinical Specimens

A total of 56 specimens of oral lesions (epithelial dysplasia and squamous cell carcinoma) were collected at the Dental Hospital of Tokyo Medical and Dental University. Pharyngeal cancers were excluded; the case summaries are shown in Supplementary Material 1. A total of 20 specimens of esophageal lesions (squamous cell carcinoma) and normal tissues were collected at Medical Hospital of Tokyo Medical and Dental University; the case summaries are shown in Supplementary Material 2. A total of 57 specimens of uterine cervical lesions (intraepithelial neoplasm and squamous cell carcinoma) were collected at Keio University Hospital; the case summaries are shown in Supplementary Material 3. The tissues were fixed in formalin and embedded in paraffin according to the routine laboratory protocol. HPV genotyping was performed as previously described[22] from the conventional cytology specimens. All experiments were approved by the ethics committees of both universities.

cDNA Microarray Analysis

Oral squamous cell carcinoma (OSCC) cells were taken from surgically excised specimens by laser capture microdissection and were subjected to cDNA microarray analysis, as previously described.[23]

Immunostaining and *In Situ* Hybridization

Immunohistochemical staining was performed using the Sequenza (Thermo Fisher Scientific, MA, USA). For antigen retrieval, the sections were autoclaved in alkaline buffer (10 mM Tris (pH = 9.0) and 1 mM EDTA) at 120 °C for 20 min. The primary antibodies used in this study were anti-Notch1 (EP1238Y, Epitomics, CA, USA); cleaved Notch1 (Val1744; D3B8, Cell Signaling, MA, USA) Notch2 (D67C8, Cell Signaling); Notch3 (D11B8, Cell Signaling); Hes1 (EPR4226, Epitomics); Hey1 (polyclonal, Millipore, MA, USA); keratin 5 (K5; EPR1600Y, Epitomics); K13 (EPR3671, Epitomics); K13 (alternative antibody, KS-1A3, Leica Microsystems, Wetzlar, Germany); K15 (EPR1614Y, Epitomics); K17 (D73C7, Cell Signaling); K17 (alternative antibody, E3, Dako, Glostrup, Denmark); K18 (DC10, Dako); pan-Keratin (AE1/AE3, Dako); Vimentin (SP20, Epitomics); E-cadherin (36/E-Cadherin, BD transduction laboratories, CA, USA); Desmoglein3 (3G133, Santa Cruz, CA, USA); p63 (4A4, Dako); β-tubulin (9F3, Cell Signaling) and β-actin (C-2, Santa Cruz). EnVision Dual Link (Dako) was used as the secondary antibody. Coloration was done in DAB substrate. For immunofluorostaining, Alexa Fluor 488 anti-rabbit IgG (Invitrogen, CA, USA) and DAPI were used. *In situ* hybridization to mouse E18.5 embryos was conducted as previously described.[24] Antibody adsorption test was performed as follows. HEK293 cells were transfected with *Notch1* or *NOTCH3* and were fixed 48 h after transfection. The anti-NOTCH1 or anti-NOTCH3 antibody (diluted 1/500) was applied to the fixed cells, respectively, and incubated for 1 h. The adsorbed supernatants were collected and used for immunohistochemical staining. The immunostaining results were compared with that using the antibody adsorbed to mock-transfected cells.

Protein Extraction from Formalin-Fixed Paraffin-Embedded Specimens

Formalin-fixed paraffin-embedded specimens were sectioned at 10 μm thick and deparaffinized. Tissues were manually dissected under a microscope. The collected tissues were heated at 95 °C for 1 h and then at 60 °C for 4 h in the protein extraction buffer (50 mM Tris (pH = 8.0), 5 mM EDTA, 2% SDS).

Genes

Mouse *Notch1* was provided by Dr J. Nye and constitutive active *Notch1* were previously described.[25] Notch extracellular domain (NECD) was created by ligating the PCR amplified *Notch1* extracellular and transmembrane regions (1 M to 1755G) into *pAcGFP1-C2* (Clontech). Human *Notch3* was provided by Dr A. Joutel. *Rbpj* cDNA was provided by the RIKEN BioResource Center (Ibaraki, Japan) courtesy of Dr T. Honjo and cloned into *pCMV-Tag4* (Stratagene, CA, USA), and dominant-negative *Rbpj (R218H)* was created by PCR mutagenesis. Dominant-negative *Dll1* (chick) was previously described.[26] Human *TP63α(TA)* was purchased from Invitrogen. *TP63α(ΔN)* was created as follows. A plasmid (*pBK-CMV-dN*) was made, which contained the sequence corresponding to the *TP63α(ΔN)*-specific N-terminal region by ligating annealed oligoniculeotides into *pBK-CMV* (Stratagene). As the N-terminal *TP63α(TA)*-specific region incidentally coincides to 5′ of MSC1 site, the N-terminal region was deleted from *TP63α(TA)* by MSC1 digestion, and the fragment was ligated into *pBK-CMV-dN*. The resulting plasmid was confirmed by DNA sequencing to carry *TP63α(ΔN)* identical to the wild type. Human *KRT13* and *KRT15* promoters were cloned by PCR from the BAC clone RP11-156A24, and human *KRT17* promoter was cloned from the BAC clone RP13-415G19, both of which were provided by the BACPAC Resources Center (CA, USA). The sequences of the PCR primers used in the cloning procedures will be provided on request. Stealth RNAs for human *NOTCH1* were purchased from Invitrogen. The sequence of the plus strand of the dsRNA is 5′-UCGCAUUGACCAUUCAAACUGGUGG-3′.

Cell Culture Experiments

GE-1, Ca9-22, HeLa and CaSki cells were provided by the RIKEN BioResource Center. HSC-3 and 293 cells were provided by the Japanese Collection of Research Bioresources (Osaka, Japan). Human foreskin (HFS) cells were purchased from Kurabo (Osaka, Japan). Transfections were performed using Lipofectamine 2000 (Invitrogen) or by calcium phosphate method. Cell proliferation was evaluated using a Cell Counting Kit (Dojindo, Kumamoto, Japan). Cells were lysed in RIPA buffer and the concentration of the protein was measured using a BCA Protein Assay Kit (Thermo Fisher Scientific, MA, USA). Western blot analysis and RT-PCR were performed according to standard protocols.[27] Three-dimensional culture was conducted using Millicell Culture Inserts (Millipore). Real-time RT-PCR was performed using a Lightcycler (Roche, Basel, Switzerland). The PCR primer sequences are as follows: hN1-5865F, 5′-CAACATCCAGGACAACATGG-3′; hN1-6093R, 5′-GGACTTGCCCAGGTCATCTA-3′; hN2-7187F, 5′-ATGCTTCCTCAAATGCTGCT-3′; hN2-7513R, 5′-TCATTTCTCTCCCGGATGAC-3′; hN3-7275F, 5′-GTCTGGGACCTCCTTCTTCC-3′; hN3-7628R, 5′-CCAAGGGTGCCTACTTGGTA-3′; hN4-6444F, 5′-TGCAGGCATATGGGATGTAA-3′; hN4-6665R, 5′-CATCCCCACAGTGGAGTTCT-3′; HES1-468F, 5′-GCGGACATTCTGGAATGACA-3′; HES1-594R, 5′-CGTTCATGCACTCGCTGAAG-3′; HEY1-485F, 5′-GATGACCGTGGATCACCTGAA-3′; HEY1-584R, 5′-CCGAAATCCCAAACTCCGATAG-3′; GAPDH-275F, 5′-GCACCGTCAAGGCTGAGAAC-3′; GAPDH-417R, 5′-ATGGTGGTGAAGACGCCAGT-3′.

Luciferase Activity Assay

KRT13, *KRT15* and *KRT17* promoter fragments were cloned as described in the Genes section, and ligated into *pGL4.10.* (Promega, WI, USA). The promoter construct of 0.1 μg, 0.1 μg of the *Notch1* construct and 0.01 μg of the *Renilla* luciferase standardization plasmid were transfected into GE-1 cells on 48-well plates and the luciferase activity was measured 48 h after transfection using a Dual-Luciferase Reporter Assay System (Promega). All transfections were done in triplicate and the experiments were repeated at least twice.

RESULTS

Expression of NOTCH1 in Basal Cells of Squamous Epithelium

In the pilot study, we screened for optimal antibodies that clearly detect an endogenous level of Notch in western blot analysis. The selected antibodies revealed that NOTCH1, NOTCH2 and NOTCH3 were expressed in primary HFS cells and HEK293 cells, whereas NOTCH4 was not detected (data not shown). This result was confirmed by RT-PCR analysis, which revealed expression of *NOTCH1*, *NOTCH2* and *NOTCH3* but not *NOTCH4* (data not shown). These (anti-NOTCH1 and anti-NOTCH3) antibodies reacted with recombinant Notch1 (mouse) and NOTCH3 (human), respectively, which were overexpressed in HEK293 cells as well as with the endogenous proteins, as revealed both by western blot analysis and immunofluorescent staining, validating their specific reactions (Supplementary Material 4A, B). We then examined their immunohistochemical expression in various human adult tissues. Distinct expression of NOTCH1 was observed in the basal cells of squamous epithelium (Figure 1a). This was consistent with the result of *in situ* hybridization, which exhibited basal-cell expression of *Notch1* in an embryonic mouse skin (Figure 1b). The NOTCH1 protein was detected mainly on the plasma membrane, which is consistent with its function as a transmembrane receptor (Figure 1a). Nuclear staining was rarely observed. Antibody adsorption test showed significantly reduced staining when the antibody was absorbed to *Notch1*-transfected cells, validating the usability in immunohistochemical detection (Supplementary Material 4C). Both cornified- and non-cornified squamous epithelia expressed NOTCH1. The expression in the esophagus and vagina appeared weaker than that in the skin and oral mucosa (Figure 1c), suggesting that the epithelium of ectodermal origin (skin, oral mucosa) expresses NOTCH1 more than that of endodermal origin (esophagus, vagina). Basal (myoepithelial) cells in the secretory glands were weakly

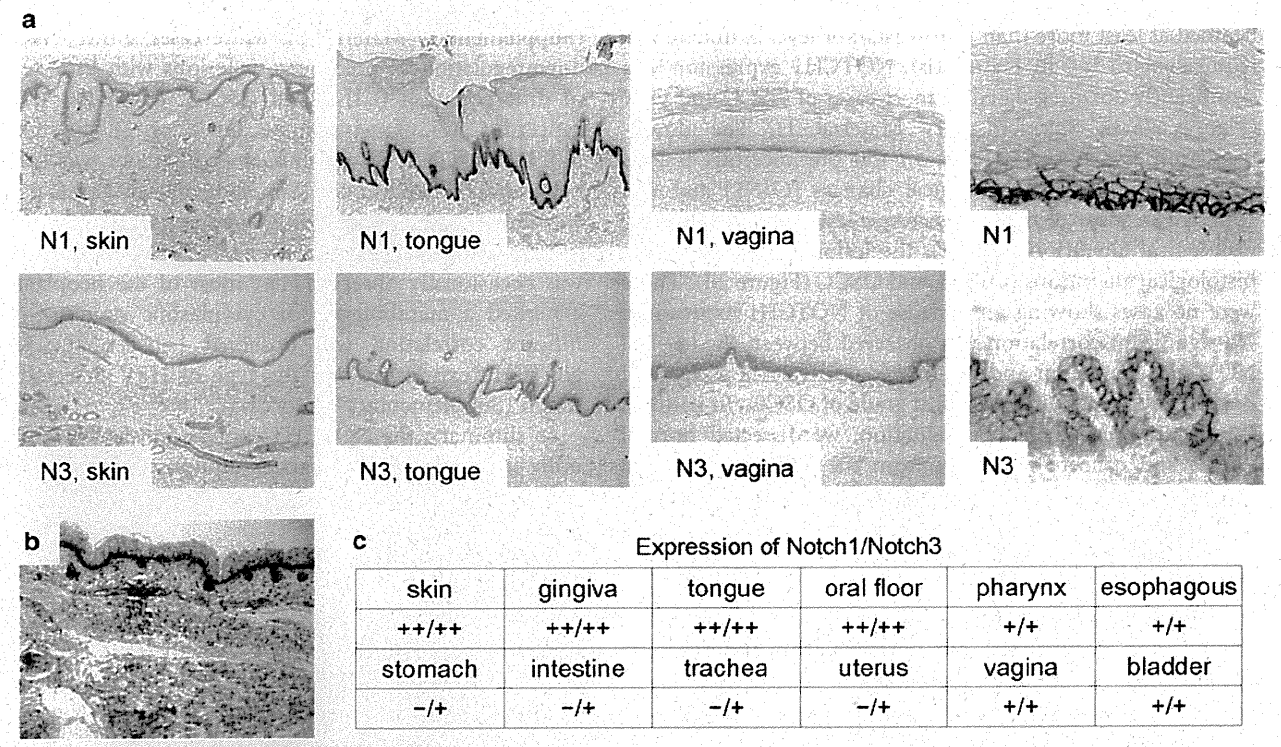

c

Expression of Notch1/Notch3

skin	gingiva	tongue	oral floor	pharynx	esophagous
++/++	++/++	++/++	++/++	+/+	+/+
stomach	intestine	trachea	uterus	vagina	bladder
−/+	−/+	−/+	−/+	+/+	+/+

Figure 1 Expression of NOTCH1 and NOTCH3 in various tissues. (**a**) Immunohistochemical staining of adult human skin, tongue and vagina shows distinct expression in the basal cells. Membrane staining pattern is obvious (right). (**b**) *In situ* hybridization on the skin of mouse E18.5 embryo, using *Notch1* RNA probe. (**c**) Simplified summary of the expression in the epithelium of each tissue.

positive for NOTCH1 (data not shown). In the uterus, the columnar epithelium, including subcolumnar reserve cells, was almost negative for NOTCH1. In the digestive tract, NOTCH1 was detected faintly only in the basal crypts (data not shown). In the subepithelial tissue, NOTCH1 was detected weakly in the vascular endothelial cells (data not shown). NOTCH3 was also expressed in the basal cells of squamous epithelium, showing membranous localization (Figure 1a). The staining pattern of NOTCH3 was a little different from that of NOTCH1, showing weak ubiquitous cytoplasmic staining also in glandular cells (data not shown). This staining in glandular cells seemed nonspecific because it did not decrease when the adsorbed antibody was used, whereas the staining in the basal cells weakened (data not shown). The NOTCH2 antibody was not applicable to immunohistochemical detection, showing no staining in any tissues (data not shown). In summary, NOTCH1 and NOTCH3 were expressed mainly in the basal cells of squamous epithelium.

NOTCH1 Expression Is Downregulated in Squamous Neoplasms

As the anti-NOTCH3 antibody yielded some nonspecific staining that would hamper correct evaluation, we determined to focus on NOTCH1 in this study and expanded our investigations to neoplasms. Because the squamous epithelia were dominant sites of NOTCH1 expression, we chose squamous neoplasms that develop at these sites and investigated whether the expression is upregulated, downregulated or unchanged. For this purpose, we collected surgical specimens of squamous cell carcinoma (cancer). To assess the contribution of NOTCH1 in cancer progression, surgical specimens of intraepithelial neoplasm (precancer) were also collected. To compensate for the organ-specific differences, specimens were collected from three different tissue sources—oral mucosa, esophagus and uterine cervix.

First we examined the NOTCH1 expression in 56 cases of oral epithelial neoplasm, including OSCC and oral intraepithelial neoplasm (OIN). We randomly collected specimens that contained normal epithelium, and the expression was evaluated by the staining intensity in individual tumor cells in comparison with that in normal basal cells within the same specimen. The distinct staining pattern with abrupt changes at the interface between normal epithelium and neoplasm enabled us to adopt this methodology. The expression was scored as being at one of five levels: level 4, upregulated expression compared with the normal basal cells; level 3, expression level similar to the normal basal cells (equivalent to '+ +' in Figure 1c); level 2, expression level less than the normal basal cells; level 1, stained only faintly

(stained at least more than fibroblasts); or level 0, undetected (equivalent to '–' in Figure 1b). NOTCH1 expression was significantly downregulated in most cases of OSCC and OIN (Figures 2a–d, Supplementary Material 1). The downregulation was observed even in the precancerous lesions with minimum histopathological changes (OIN1) and was apparent in most of the precancerous lesions with moderate histological alterations (OIN2), the lesions with prominent histological alterations (OIN3), and OSCC (Figure 2d). There were no cases showing an increase of NOTCH1 expression. No significant correlation was observed between the level of NOTCH1 expression and the histological variations of OIN or the histological differentiation grade of OSCC. To confirm the immunohistochemical evaluation, we dissected normal tissues and cancers separately from the sections, extracted proteins and conducted western blot analysis. In all, 4 out of 10 cases were informative, all of which showed reduced NOTCH1 expression in cancer, normalized to keratin 5 (Figure 2e). This result is consistent with the immunohistochemical observations. Proteins of sufficient amount and quality were not obtained from the other six specimens, probably due to the fixation period. The downregulation of *NOTCH1* in OSCC was also confirmed by cDNA microarray analysis of 41 OSCC *vs* 7 normal oral epithelia ($P<0.001$), with the average expression in OSCC reduced to 0.43-fold compared with the normal control (Figure 2f). The cDNA microarray showed that *NOTCH2* and *NOTCH3* were also downregulated in OSCC to 0.78-fold and 0.83-fold, respectively (data not shown).

Next, we examined the immunohistochemical expression of NOTCH1 in squamous cell carcinoma of esophagus (ESCC; Supplementary Material 2 and 5). Downregulation was evident in 17 out of 20 cases while weak expression remained. The remaining three cases retained a considerable expression, but there were no cases with NOTCH1 upregulation.

Next, we examined the immunohistochemical expression of NOTCH1 in uterine cervical lesions (Supplementary Material 3, 6). NOTCH1 expression tended to be downregulated in cervical intraepithelial neoplasm (CIN) and cervical squamous cell carcinoma (CSCC). However, more than 50% of the cases retained considerable expression (Supplementary Material 6). More cases showed NOTCH1 downregulation in precancerous lesions with little tendency of differentiation (CIN3 and CSCC), compared with precancerous lesions with some tendency of differentiation (CIN1 or CIN2). No significant difference was observed between CIN3 and CSCC (Supplementary Material 6). There was not a single case showing apparent NOTCH1 upregulation in the individual cancer cells. Indistinct nuclear staining was occasionally observed, but most of the neoplastic cells exhibited a membranous or cytoplasmic staining. No significant correlation was observed between the level of NOTCH1 expression and the type of HPV detected in the lesion (Supplementary Material 3).

In summary, the NOTCH1 expression was downregulated both in precancer and cancer of non-cornified squamous epithelium.

NOTCH1 Regulates the Differentiation of Squamous Epithelium

The fact that NOTCH1 was downregulated not only in cancer but also in precancer suggests that aberrant NOTCH1 expression associates with changes of epithelial properties observed both in precancers and cancers. The essential properties that discriminate cancer from precancer are invasion and resultant metastasis, and our data suggest that the downregulation of NOTCH1 may not contribute to these cancer-specific events. In contrast, dysregulation of differentiation is a common feature observed both in cancer and precancer, appearing as abnormality of cell alignment, stratification and keratinization. Considering that Notch governs cell-to-cell signaling, we hypothesized that reduction of Notch signaling might affect the cell-to-cell-based regulation of epithelial differentiation. To test this hypothesis, we conducted cell culture experiments. First, we examined Notch expression in cell lines derived from cervical cancers (HeLa, CaSki), oral cancers (BHY, Ca9-22, HSC-3) and primary HFS cells. Western blot analysis revealed that both NOTCH1 and NOTCH3 were expressed most abundantly in the normal cells, and variably, but at much lower levels, in the cancer cell lines (Figure 3a), which is a finding consistent with the observation that NOTCH1 expression was downregulated in squamous neoplasms. NOTCH2 was considerably expressed

Figure 2 Expression of NOTCH1 in oral squamous cell carcinoma (OSCC, cancer) and oral intraepithelial neoplasm (OIN, precancer). (**a**) OSCC associated with OIN. Low-magnification view and the highlighted borders of the lesion (A, B). NOTCH1 expression is significantly reduced in OIN (A) and OSCC (B). Clear demarcations of NOTCH1 expression are seen, which coincides with the border of the lesion. Scale bar, 0.5 mm. (**b**) OIN1 (mild epithelial dysplasia). NOTCH1 is significantly downregulated even in this lesion with minimum histological change, and the border of NOTCH1 expression coincides with the border of the lesion. Scale bar, 0.5 mm. (**c**) Papillary-type OSCC. Low-magnification view with the highlighted border of the lesion (C). Downregulation of NOTCH1 is evident. Scale bar, 0.5 mm. (**d**) Numbers of cases (and percentage) with reduction of NOTCH1 expression. G1, well-differentiated; G2, moderately differentiated; G3, poorly differentiated OSCCs. (**e**) Western blot analysis using surgical specimens. Formalin-fixed paraffin-embedded tissues were separately dissected from normal (N) and cancer (C) tissues, and the proteins were extracted. A sufficient amount of protein was obtained from 4 out of 10 cases, in which NOTCH1 expression was reduced in cancer (Case #1 to #4). Keratin 5 (K5) was used for standardization. Case #5 is shown as an example of a non-informative case. (**f**) cDNA microarray analysis of 41 OSCC and 7 normal control epithelia. Vertical axis corresponds to globally normalized signal intensity of *NOTCH1* mRNA expression. *NOTCH1* is significantly downregulated in OSCC compared with normal epithelium (*$P<0.001$). Short bars, expression in each case; long bars, mean; error bars, s.e.

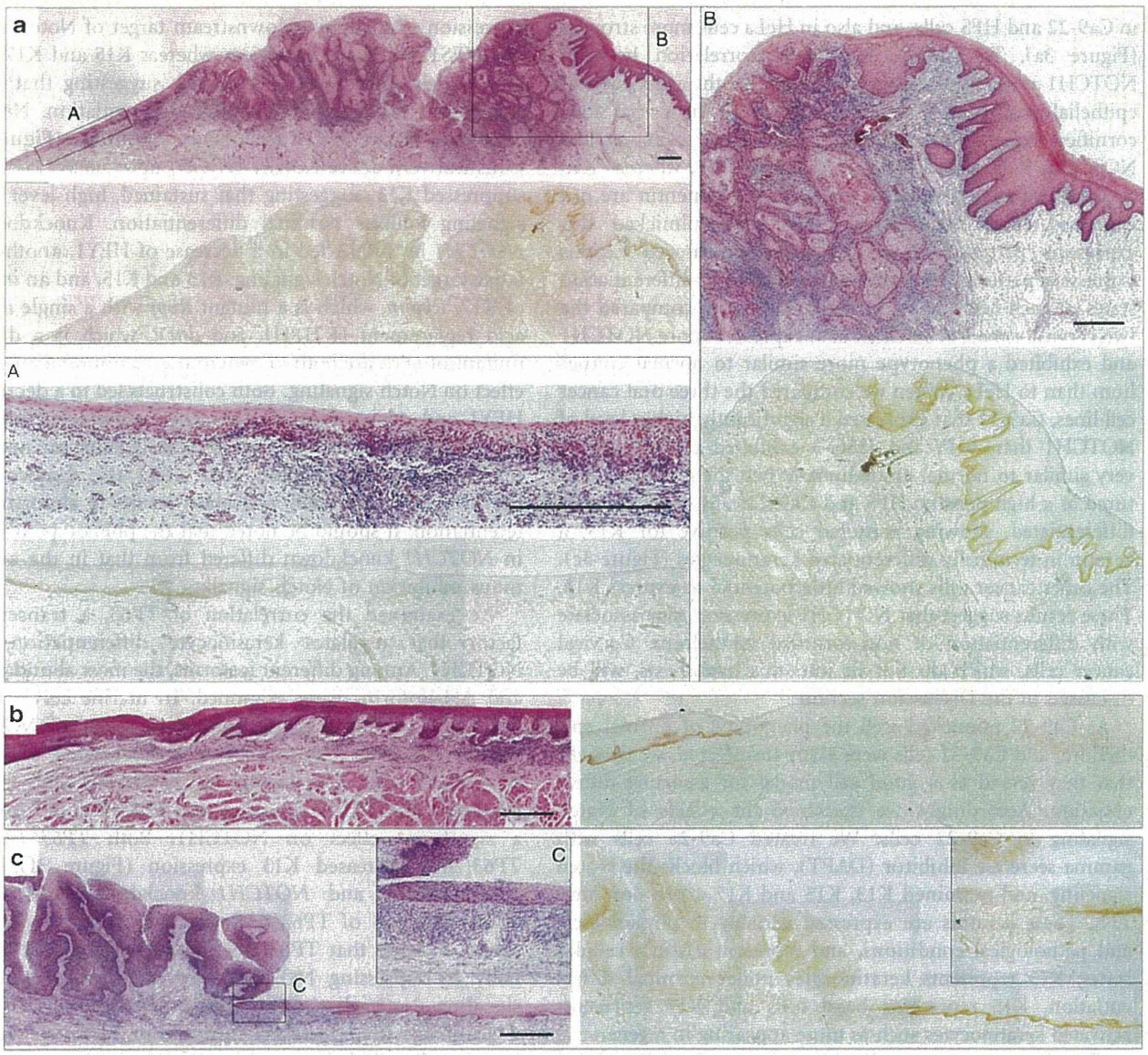

d

OIN		
OIN1	OIN2	OIN3
8/10 (80%)	12/13 (92%)	10/10 (100%)
OSCC		
G1	G2	G3
14/16 (88%)	8/8 (100%)	2/3 (67%)

e

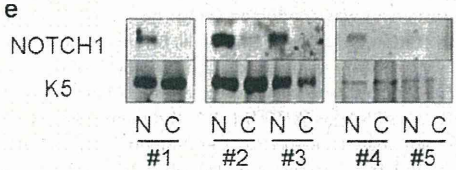

f

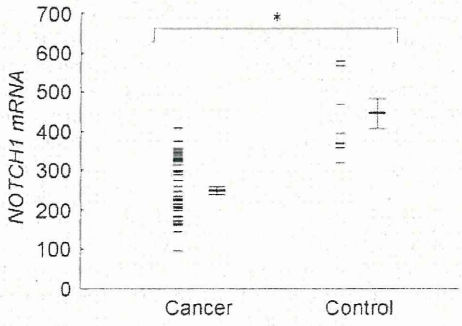

in Ca9-22 and HFS cells, and also in HeLa cells more strongly (Figure 3a). To assess the possible correlation between NOTCH1 and differentiation, we examined the expression of epithelial markers in these cells (Figure 3b). In normal non-cornified squamous epithelium, the basal cells express NOTCH1, K15, K19, CDH1, DSG3 and TP63, whereas K16 and K17 expression is weak, and K18 and vimentin are not expressed (data not shown). HFS cells mimicked this expression pattern. The cancer cell lines showed various expression patterns, reflecting the diversities in differentiation states of each cell line (Figure 3b). When we compared the two cervical cancer cell lines, CaSki expressed more NOTCH1 and exhibited a phenotype more similar to normal epithelium than to HeLa. When we compared the three oral cancer cell lines, Ca9-22 that expressed a significantly higher level of NOTCH1 than BHY and HSC-3 exhibited the phenotype very similar to normal epithelium. When the cells were cultured at a high density, HFS and Ca9-22 cells spontaneously differentiated, showing scattered cells positive for K13, a keratin in terminally differentiated keratinocytes (Figure 3c). The other cancer cells showed little potential to express K13. These results suggest that NOTCH1 expression may associate with differentiation of non-cornified epithelium. Cervical cancer cells, which do not fit into this hypothesis, will be discussed in the Discussion section.

As Ca9-22 mimicked well the phenotype of normal epithelium, and Ca9-22 cells were easily transfected, we thought that they served as a good cell model for assessing differentiation. Accordingly, we examined the effects of Notch signaling in Ca9-22 cells. We treated Ca9-22 cells with gamma-secretase inhibitor (DAPT), which blocks the Notch signaling, and examined K13, K15 and K17 expression after 72 h. These keratins are expressed variably in physiological and pathological conditions, and represent distinct cellular states; K13 represents keratinocytes under terminal differentiation, K15 represents basal cells and K17 represents activated keratinocytes such as those appearing in regenerative epithelium and cancer. DAPT treatment led to reduced expression of a putative downstream target of Notch signaling, HES1, and K13 expression, whereas K15 and K17 levels were largely unchanged (Figure 3d), suggesting that Notch signaling is necessary for terminal differentiation. Next the cells were transfected with various constructs (Figure 3e). Constitutively, active Notch1 (NICD) upregulated HES1 and suppressed K13, suggesting that sustained, high-level Notch signaling inhibits terminal differentiation. Knockdown of *NOTCH1* by siRNA led to a decrease of HEY1, another putative target of Notch signaling, K13 and K15, and an increase of K17. *Rbpjm*, which is a mutant *Rbpj* with a single amino-acid replacement (R218H), and *dnDl*, which is a deletion mutant of *Dll1*, are both known to pose a dominant-negative effect on Notch signaling. Both constructs led to a decrease of HEY1 and an increase of K13. These results indicate that proper expression of NOTCH1 and its signaling are necessary for terminal differentiation, and either the absence of its signaling or its untimely activation results in abnormal differentiation. It should be noted that the phenotype observed in *NOTCH1* knockdown differed from that in the autonomous inhibition of Notch signaling.

We examined the correlation of TP63, a transcription factor that regulates keratinocyte differentiation, with NOTCH1. Among different isoforms, the most abundant TA- and ΔN-isoforms were examined. In uterine cervical cells, TP63(ΔN) acts as a transcriptional repressor of *NOTCH1*, which results in maintenance of self-renewing capacity.[28] In Ca9-22 cells, transfection of *TP63(ΔN)* only slightly decreased NOTCH1 expression and *TP63(TA)* did not have a significant effect on NOTCH1. Both *TP63(TA)* and *TP63(ΔN)* decreased K13 expression (Figure 3f). *NICD* overexpression and *NOTCH1* knockdown both led to downregulation of TP63(ΔN) and K13 (Figure 3g). These results indicate that TP63(ΔN) inhibits differentiation partially by repressing NOTCH1 expression, whereas Notch signaling also mediates TP63(ΔN) expression.

To further investigate the contribution of Notch signaling in regulation of keratin subtype expression, we conducted

Figure 3 NOTCH1 regulates keratin expression. (**a**) Expression of NOTCH1, NOTCH2 and NOTCH3 in cervical cancer cell lines (HeLa, CaSki), oral cancer cell lines (BHY, Ca9-22, HSC-3) and primary human foreskin (HFS) cells, as revealed by western blot. All the antibodies recognize an epitope in the intracellular domain. Most proteins were detected as a furin-cleaved form containing the transmembrane and intracellular domains. A small amount of full-length protein was also detected. Gamma-secretase-cleaved C-terminal fragment (NICD) was not observed in NOTCH1 and NOTCH3 blots. (**b**) Expression of various keratins (K), vimentin (Vim), E-cadherin (Cdh1), desmoglein 3 (Dsg3) and TP63 in various cells, as revealed by western blot. As the full-length NOTCH1 was observed at a much weaker intensity and in proportion to the intensity of the 120 kDa protein, only the 120 kDa protein of NOTCH1 is shown. (**c**) K13 expression in Ca9-22 and HFS cells cultured at a high density. Immunofluorostaining was conducted using the secondary antibody labeled by Alexafluor 488. The nuclei were counterstained by DAPI. K13-expressing cells appear in a scattered manner. HeLa, CaSki, BHY and HSC-3 showed no K13 expression. (**d**) Ca9-22 cells were treated with only DMSO or 2.5 μM DAPT at 80% confluency and were cultured for 72 h. An equal amount of protein was subjected to western blot analysis for keratins (K), HES1, HEY1 and β-tublin (βTub). (**e**) Ca9-22 cells were transfected at 30% confluency with an empty plasmid (Ctrl), NICD, dominant-negative RBPJ (R218H, RBPJm), dominant-negative Dll1 (dnDl) or siRNA for *NOTCH1* (*siN1*) and were cultured for 72 h. (**f**) Ca9-22 cells were transfected with *TP63(TA)* or *TP63(ΔN)* and were incubated for 72 h. Western blot analysis revealed the endogenous expression of TP63 (ΔN), but not TP63 (TA). NOTCH1 was only slightly downregulated by TP63 (ΔN). K13 was downregulated both by TP63 (TA) and TP63 (ΔN). (**g**) Ca9-22 cells were transfected with *NICD* or siRNA for *NOTCH1* and were incubated for 72 h. Both *NICD* and *siN1* downregulated TP63 and K13. (**h**) Luciferase reporter assay for human *KRT13*, *KRT15* and *KRT17* promoters. The promoter construct plus of 0.1 μg and 0.1 μg of the Notch1 construct and 0.01 μg of the *Renilla* luciferase standardization plasmid (*pEF-RL*). Transfections were done into GE-1 cells on 48-well plates and the luciferase activity was measured 48 h after transfection using Dual-Luciferase Reporter Assay System (Promega). The error bars denote standard errors. rlu; relative luciferase unit.

promoter analysis of the keratin genes using GE-1 cells that were established from normal mouse gingival epithelium. We co-transfected the cells with *Notch1*, *NICD* or *NECD*, and the luciferase reporter constructs for *KRT13*, *KRT15* or *KRT17* promoters. NECD is a membrane-tethered Notch1 extracellular domain whose intracellular domain was replaced by AcGFP. Notch1 increased the *KRT13* promoter activity while NICD decreased it. NECD decreased the *KRT15* promoter activity and slightly increased the *KRT17* promoter activity (Figure 3h). These results suggest that NOTCH1-expressing cells have more potential to differentiate, but Notch signaling itself autonomously inhibits differentiation and directs the cell to maintain basal-cell phenotype.

Next we examined the effect of *NOTCH1* knockdown in normal epithelial cells using the primary HFS cells. The knockdown efficiency was more than 90% as revealed by

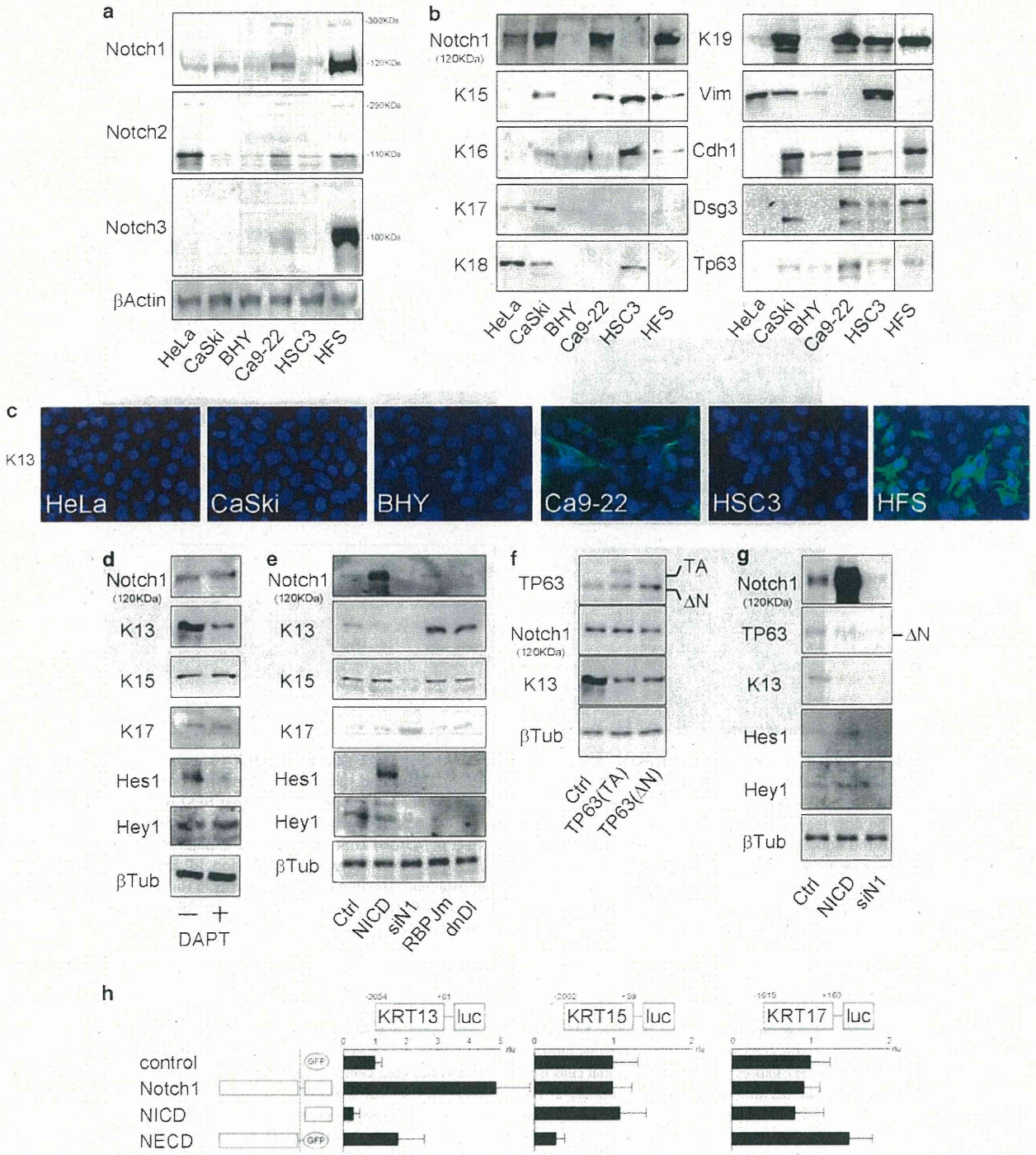

western blot analysis (Figure 4a). *NOTCH1* knockdown significantly suppressed the expression of *HEY1*, whereas *HES1* showed only slight (20%) reduction, as revealed by real-time PCR (Figure 4b, real-time PCR data are not shown). Cell proliferation was not altered by *NOTCH1* knockdown (data not shown). The total amount of keratin protein was unchanged, and vimentin was not induced by *NOTCH1* knockdown (Figure 4c). *NOTCH1* knockdown led to downregulation of K13 and K15, and upregulation of K17. Immunocytostaining using the anti-K13 antibody revealed that *NOTCH1* knockdown resulted in a decrease both of the staining intensity in individual cells and of the number of stained cells (Figure 4d). The expression of CDH1 (E-cadherin), DSG3 (desmoglein 3) and TP63 was not significantly

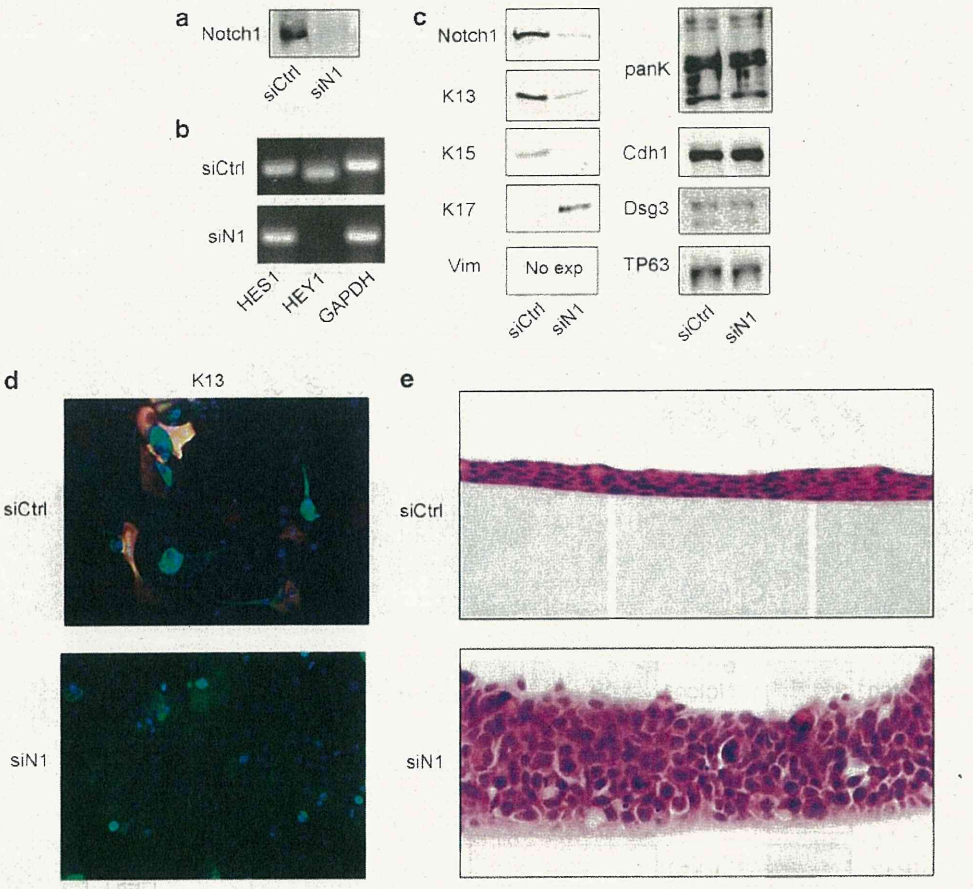

Figure 4 Notch1 knockdown in primary foreskin (HFS) cells results in immature epithelium. (**a**) Efficiency of *NOTCH1* knockdown. HFS cells were transfected with negative control siRNA (*siCtrl*) or siRNA for *NOTCH1* (*siN1*) were incubated for 7 days and subjected to western blot analysis. (**b**) Effect of *NOTCH1* knockdown on the target genes. Real-time RT-PCR revealed that *HEY1* was almost completely suppressed, whereas *HES1* was downregulated only by 20% (data not shown). The post-real-time PCR samples were diluted and amplified for an additional two cycles in order to make them visible on gel electrophoresis. Thus this figure actually shows conventional RT-PCR. (**c**) The effect of *NOTCH1* knockdown on the expression of keratinocyte differentiation markers. K, keratin; Vim, vimentin; panK, pan-keratin; Cdh1, E-cadherin; Dsg3, desmoglein 3; No exp, no expression. (**d**) Expression of K13 in HFS cells transfected with *siCtrl* or *siN1* 7 days after transfection, revealed by immunofluorostaining. The fluorescence intensity in the individual cells and the number of positively stained cells decreased in the siN1-transfected cells. (**e**) Vertical sections of three-dimensionally cultured HFS cell layers, stained with hematoxylin and eosin. Cells were transfected and seeded in Millicell culture inserts and cultured for 10 days.

Figure 5 Immunohistochemical expression of NOTCH1, K13, K15 and K17 in squamous neoplasms. (**a**) In this OIN case, the lesion shows concomitant downregulation of NOTCH1, K13 and K15, with complimentarily induced expression of K17. Scale bar, 0.5 mm. (**b**) In this CIN case showing condylomatous proliferation, the level of NOTCH1 expression in the individual cells is retained, and basaloid cells expressing NOTCH1 and K15 expand in the whole layer. K17 induction is faint. Scale bar, 0.5 mm. (**c**) Schematic summary of the immunohistochemical expression of NOTCH1 and K13 in various squamous neoplasms. Each group of the lesions is plotted by the average scores of NOTCH1 and K13 expression. OIN, oral intraepithelial neoplasm; OSCC, squamous cell carcinoma of the oral cavity; ESCC, squamous cell carcinoma of the esophagus; CIN, cervical intraepithelial neoplasm; CSCC, squamous cell carcinoma of the cervix.

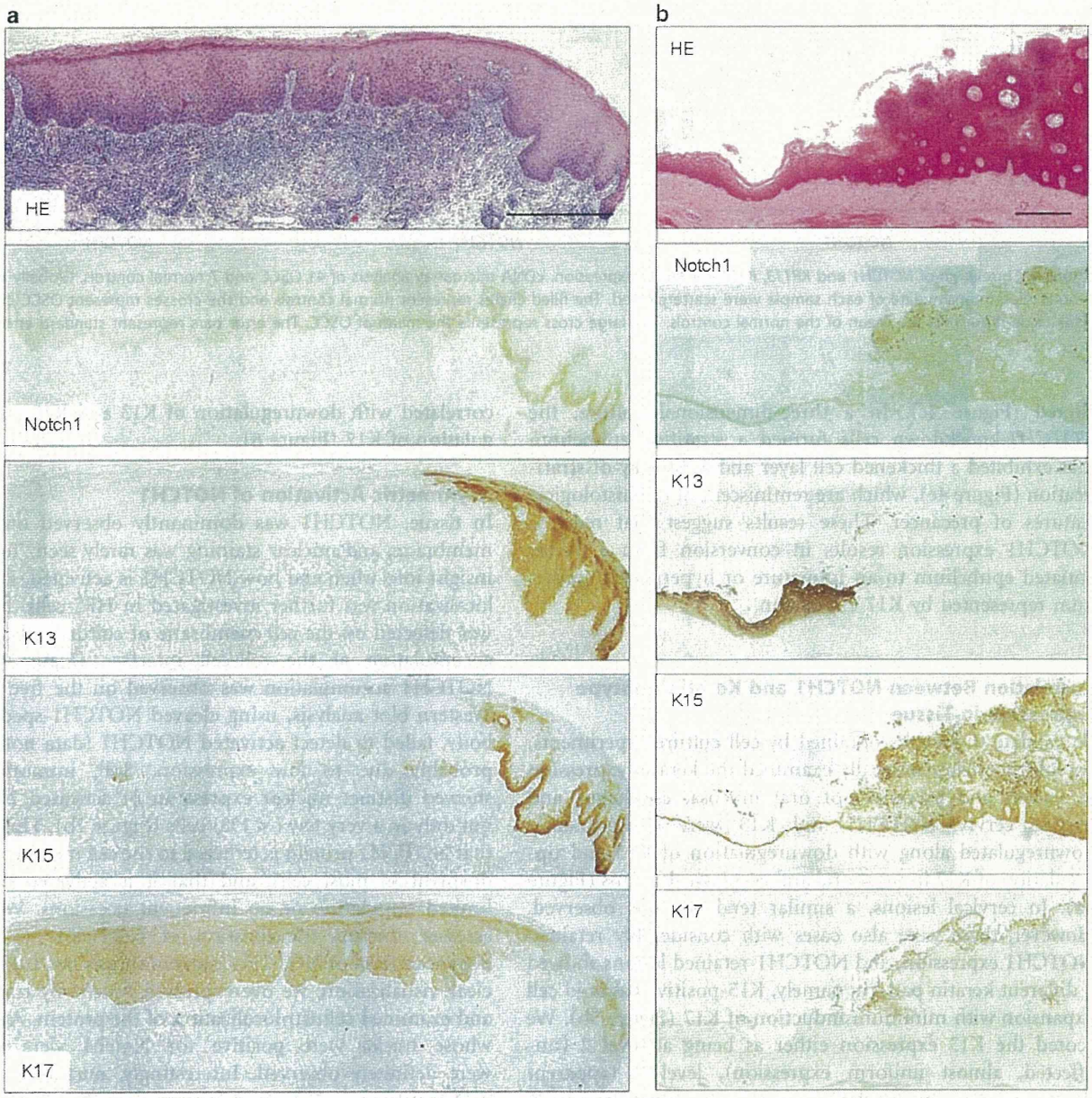
a
HE
Notch1
K13
K15
K17
b
HE
Notch1
K13
K15
K17

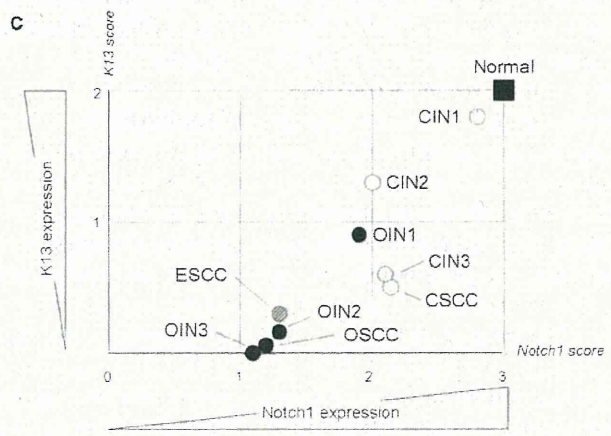
c
K13 score
K13 expression
Normal
CIN1
CIN2
OIN1
CIN3
CSCC
ESCC
OIN2
OIN3
OSCC
Notch1 score
Notch1 expression
0
1
2
3

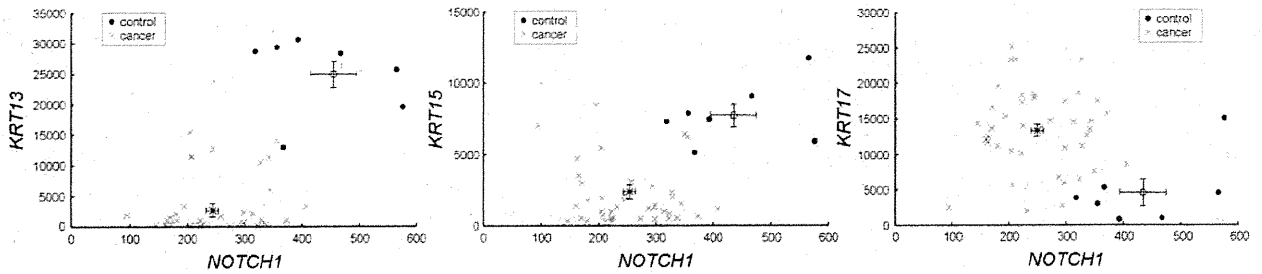

Figure 6 Correlation of *NOTCH1* and *KRT13*, *KRT15* or *KRT17* expression. cDNA microarray analysis of 41 OSCC and 7 normal controls. Globally normalized hybridization intensity data of each sample were scatterplotted. The filled circles represent normal controls and the crosses represent OSCC cases. The blank circle represents the mean of the normal controls. The large cross represents the mean of OSCC. The error bars represent standard errors.

altered (Figure 4c). In a three-dimensional culture, the *NOTCH1*-knockdown cells formed a stratified epithelium that exhibited a thickened cell layer and a disarray of stratification (Figure 4e), which are reminiscent of the histological features of precancer. These results suggest that reduced NOTCH1 expression results in conversion from a differentiated epithelium to an immature or hyperplastic epithelium represented by K17 expression.

Correlation Between NOTCH1 and Keratin Subtype Expression in Tissue

To validate the results obtained by cell culture experiments, we immunohistochemically examined the keratin expression in cancer and precancer of oral mucosa, esophagus and uterine cervix. NOTCH1 and K13 were concomitantly downregulated along with downregulation of K15 and upregulation of K17 in most oral and esophageal lesions (Figure 5a). In cervical lesions, a similar tendency was observed. However, there were also cases with considerably retained NOTCH1 expression, and NOTCH1-retained lesions showed a different keratin pattern, namely, K15-positive basaloid cell expansion with minimum induction of K17 (Figure 5b). We scored the K13 expression either as being at level 2 (unaffected, almost uniform expression), level 1 (apparent downregulation but patchy expression remaining) or level 0 (almost complete loss of expression), and analyzed the correlation of these three expression levels with the NOTCH1 scores. Loss of K13 expression was observed in accordance with NOTCH1 downregulation (Figure 5c). The average scores of K13 and NOTCH1 decreased in accordance with the grades of OIN and CIN, although the high-grade lesions (OIN2, OIN3, CIN3) showed scores similar to those of OSCC or CSCC (Figure 5c), indicating that these precancers and cancers in each site are essentially the same lesions in the context of NOTCH1 and K13 expression. The cervical lesions, especially low-grade CIN, tended to show more NOTCH1 and K13 expression. Correlation between NOTCH1 expression and keratin expression was further assessed in oral cancers using microarray data. Scatter plots revealed that the downregulation of NOTCH1 in cancer correlated with downregulation of K13 and K15, and upregulation of K17 (Figure 6).

Asymmetric Activation of NOTCH1

In tissue, NOTCH1 was dominantly observed on the cell membrane, and nuclear staining was rarely seen. To gain an insight into when and how NOTCH1 is activated, its cellular localization was further investigated in HFS cells. NOTCH1 was detected on the cell membrane of culture cells, showing accumulation at the cell-cell interface (Figure 7a). No NOTCH1 accumulation was observed on the free surfaces. Western blot analysis, using cleaved NOTCH1-specific antibody, failed to detect activated NOTCH1 (data not shown), probably due to low expression. Still, immunostaining showed distinct nuclear expression of activated NOTCH1, but only in a very few (<1%) cells (Figure 7b). This suggests that NOTCH1 protein is tethered to the cell membrane and is dormant in most cells, and that it is activated only in a limited population or on infrequent occasions. We further assessed nuclear translocation of NOTCH1. As the endogenous level of NOTCH1 expression was not sufficient for clear visualization, we overexpressed *Notch1* by transfection and examined cellular localization of the protein. Again, cells whose nuclei were positive for Notch1 were rare but were definitely observed. Interestingly, nuclear localization of Notch1 was occasionally observed in one of two neighboring cells, which appeared as postmitotic daughter cells (Figure 7c).

DISCUSSION

We demonstrated that NOTCH1 is expressed predominantly in the basal cells of normal squamous epithelium. Contrary to our findings, previous reports had documented the expression in both basal and suprabasal layers of the skin[4,21] and in the uterine cervix,[15,16] as well as in the suprabasal layer of the cornea,[29] but we believe the present study correctly demonstrates the basal-cell dominant NOTCH1 expression in human squamous epithelium and its neoplasms. The most prominent feature that supports the validity of our immunohistochemical examination is the sharp demarcation of NOTCH1 expression that matched to the border between